Glial-dependent clustering of voltage-gated ion channels in Drosophila precedes myelin formation

Simone Rey[#1], Henrike Ohm[#1], Frederieke Moschref[1,2], Dagmar Zeuschner[3], Marit Praetz[1], and Christian Klämbt *[1]

Affiliations:

[1] Institut für Neuro- und Verhaltensbiologie; Röntgenstraße 16, D-48149 Münster, Germany.

[2] present address: Max-Planck Institut für Multidisziplinäre Naturwissenschaften; Hermann-Rein-Str. 3, D-37075 Göttingen, Germany.

[3] Max-Planck Institut für molekulare Biomedizin; Wissenschaftliches Service-Labor für Elektronenmikroskopie; Röntgenstraße 20, D-48149 Münster, Germany.

# Equal contribution

* corresponding author: klaembt@uni-muenster.de

Abstract

Neuronal information conductance often involves the transmission of action potentials. The spreading of action potentials along the axonal process of a neuron is based on three physical parameters: The axial resistance of the axon, the axonal insulation by glial membranes, and the positioning of voltage-gated ion channels. In vertebrates, myelin and channel clustering allow fast saltatory conductance. Here we show that in *Drosophila melanogaster* voltage-gated sodium and potassium channels, Para and Shal, co-localize and cluster in an area resembling the axon initial segment. The local enrichment of Para but not of Shal localization depends on the presence of peripheral wrapping glial cells. In larvae, relatively low levels of Para channels are needed to allow proper signal transduction and nerves are simply wrapped by glial cells. In adults, the concentration of Para increases and is prominently found at the axon initial segment of motor neurons. Concomitantly, these axon domains are covered by a mesh of glial processes forming a lacunar structure that possibly serves as an ion reservoir. Directly flanking this domain glial processes forming the lacunar area appear to collapse and closely apposed stacks of glial cell processes can be detected, resembling a myelin-like insulation. Thus, Drosophila development may reflect the evolution of myelin which forms in response to increased levels of clustered voltage-gated ion channels.

One-Sentence Summary: Evolution of saltatory conductance is mirrored in fly development where glia dependent clustering of voltage-gated ion channels precedes myelination.

Introduction

A functional nervous system requires the processing and transmission of information in the form of changing membrane potentials. To convey information along axons, neurons generate action potentials by opening of evolutionarily conserved voltage-gated sodium and potassium channels (Moran et al., 2015). Once an action potential is generated, it travels towards the synapse and the speed of information transfer is of obvious importance. It is long established that axonal conductance velocity depends on the resistance within the axon, which inversely correlates with its diameter. In addition, it depends on the resistance across the axonal membrane, which is increased by extensive glial wrapping. Furthermore, spacing of voltage-gated ion channels contributes to axonal conduction velocity (Eshed-Eisenbach and Peles, 2019; Freeman et al., 2016; Hodgkin and Huxley, 1952).

In vertebrates, unmyelinated axons generally have a small diameter with evenly distributed voltage-gated ion channels along their plasma membrane, and in consequence their conductance velocity is slow (Castelfranco and Hartline, 2015). To speed up conductance, axons grow to a larger diameter and show a clustering of voltage-gated ion channels at the axon initial segment and the nodes of Ranvier. Together with the insulating glial-derived myelin sheet, this allows fast saltatory conductance (Arancibia-Cárcamo et al., 2017; Castelfranco and Hartline, 2015; Cohen et al., 2019; Dutta et al., 2018; Eshed-Eisenbach and Peles, 2019).

In invertebrates, mechanisms to increase conductance speed are thought to be limited by radial axonal growth, as seen in the giant fiber system of Drosophila or the giant axon of the squid (Allen et al., 2006; Hartline and Colman, 2007). No saltatory conductance has been described for invertebrates and it is assumed that voltage-gated ion channels distribute relatively evenly

along axonal membranes. Nevertheless, myelin-like structures were found in several invertebrate species, including annelids, crustacean and insects (Coggeshall and Fawcett, 1964; Davis et al., 1999; Günther, 1976; Hama, 1959; 1966; Hess, 1958; Heuser and Doggenweiler, 1966; Levi et al., 1966; Roots, 2008; Roots and Lane, 1983; Wigglesworth, 1959; Wilson and Hartline, 2011a; b). However, it is unknown whether such myelin-like structures also impact the distribution of ion channels.

To address how glial cells affect axonal conductance velocity we turned to Drosophila. In the larvae, peripheral axons are engulfed by a single glial wrap resembling Remak fibers in the mammalian PNS (Matzat et al., 2015; Nave and Werner, 2014; Stork et al., 2008). In addition to insulating axons, we found that glial cells promote radial axonal growth. In the absence of wrapping glia axons are not only thin, but they are also characterized by a severe reduction in conductance velocity, which is stronger than predicted by the reduced axonal diameter (Hodgkin and Huxley, 1952; Kottmeier et al., 2020). Thus, wrapping glial cells might control localization of voltage-gated ion channels along the axonal plasma membrane.

Results

Distribution of the voltage-gated sodium channel Para

The Drosophila genome harbors only one voltage-gated sodium channel called Paralytic (Para), which is required for the generation of all action potentials (Kroll et al., 2015). To study the localization of Para and to test whether Drosophila glia affects its localization we and others tagged the endogenous *para* locus with all predicted isoforms being modified (Ravenscroft et al., 2020; Venken et al., 2011) (Figure 1A). In $para^{mCherry}$ flies, monomeric Cherry (mCherry) is inserted close to the Para N-terminus (Figure 1A). Homozygous or hemizygous $para^{mCherry}$ flies are viable with only mildly affected channel function (Figure 1B) (Ravenscroft *et al.*, 2020; Venken *et al.*, 2011). $Para^{mCherry}$ localizes along many CNS and PNS axons of the larval nervous system (Figure 1C-figure supplement 1A-C) (Ravenscroft *et al.*, 2020; Venken *et al.*, 2011).

To independently assay Para localization, we generated antibodies against an N-terminal epitope shared by all predicted Para isoforms (Figure 1A). In western blots, anti-Para antibodies detect a band of the expected size (>250 kDa), which is shifted towards a higher molecular weight in protein extracts of homozygous $para^{mCherry}$ animals (Figure 1-figure supplement 1D). Immunohistochemistry detects Para localization in control first instar larvae but not in age matched *para* null mutant animals, further validating the specificity of the antibodies (Figure 1D-E'). Whereas the pre-immune serum fails to detect any specific proteins (Figure 1F), anti-Para antibody staining of third instar larval filets revealed the localization of Para in the CNS and the PNS (Figure 1G) similar to what was noted for $Para^{mCherry}$ localization (Figure 1C). Thus, we anticipate that endogenously mCherry-tagged Para protein reflects the wild typic Para localization.

To test a possible differential distribution of Para in either sensory or motor axons, we utilized RNAi to remove *mCherry* expression in heterozygous *para*^{mCherry} females. This leaves the wild type *para* allele intact and circumvents the early lethal phenotype associated with loss of *para*. Knockdown of *mCherry* expression in glutamatergic motor neurons (Mahr and Aberle, 2006) reveals *para*^{mCherry} expression in cholinergic sensory neurons of third instar larvae. Here, Para appears to evenly localize along the abdominal nerves and is found at many processes within the CNS (Figure 2A). In contrast, silencing *para*^{mCherry} in cholinergic neurons (Salvaterra and Kitamoto, 2001) reveals a predominant localization of Para in an axonal segment of motor axons at the PNS/CNS boundary of third instar larvae (Figure 2B), as suggested before (Ravenscroft *et al.*, 2020).

Differential localization of voltage-gated potassium channels

Several genes encode voltage-gated potassium channels. Using endogenously tagged proteins, we find the Shaker potassium channel mostly in the synaptic neuropil regions (Figure 2C). The distribution of Shab resembles Para^{mCherry} localization in sensory axons (Figure 2A,D), whereas Shal localizes in a pattern similar to Para localization on motor axons (Figure 2B,E). Thus, Drosophila larval motor axons appear to have an axonal segment resembling the vertebrate axon initial segment (AIS) harboring both voltage-gated sodium and potassium channels.

We then analyzed the localization of Para in the adult CNS. Here, too, global Para localization, as detected by anti-Para antibodies, matched the Para^{mCherry} signal (Figure 2F,G). To differentiate between Para expression in motor and sensory neurons we employed the recently developed FlpTag technique (Fendl et al., 2020). Here, cell type specific expression of the Flp

recombinase induces the inversion of a GFP-encoding exon located in the gene of interest. In *para*^{FlpTag} flies (Fendl *et al.*, 2020), Flp expression in all motor neurons, results in strong labeling of Para localization at a small part of the axon as it leaves the neuropil (Figure 2H,H', arrowheads), indicating that an axon initial segment is also found in adult motor axons. In contrast, expression of Flp in all sensory neurons using *Chat-Gal4 UAS-flp*, reveals an even Para decoration of axons as they enter the CNS which fades out when axons reach into the neuropil (Figure 2I,I', arrows).

High-resolution imaging reveals clustered localization of Para along motor axons

To obtain a higher spatial resolution of Para distribution, we used high-resolution Airyscan microscopy. In adult nerves, Para^{mCherry} localization distal to the AIS is found in a clustered arrangement (Figure 3A-B', arrowheads). To exclude that cluster formation is due to the fluorescence protein moiety, we performed anti-Para immunohistochemistry on primary Drosophila neural cells in culture, where axons form small fascicles with few accompanying glial cells (Figure 3C,C'). When such cultures are stained for Para distribution, we find Para channels localized in small clusters with a spacing of about 0.6-0.8 µm. However, in these neuronal cultures we cannot clearly define the number of Para expressing axons in a fascicle.

To further improve spatial resolution, we combined high-resolution imaging with the FlpTag labeling method. We restricted Flp expression to only one motor neuron in each larval hemineuromer using *94G06-Gal4* (Jenett et al., 2012; Pérez-Moreno and O'Kane, 2019), which results in the expression of GFP-tagged Para channels in only a single neuron. Whereas weak expression is noted around the nucleus strong expression is seen in the axon initial segment

(Figure 3D, arrow, asterisks). Flanking the strong expression along the AIS, a clustered localization of $Para^{GFP}$ could be noted (Figure 3E, arrowheads). Further super-resolution imaging of single motor axons decorated with GFP-tagged Para showed an average spacing of 0.620 µm (Figure 3F,F',G, n=91 clusters on 3 axons, quantification using Fiji). Interestingly, Para clusters appear to be organized along lines at the motor axon which was also found when analyzing the distribution of Para at the electron microscopic level (see below).

In sensory neurons increased Para localization is found at dendrites and the AIS

Having shown that in motor axons Para is concentrated in a clustered arrangement in an axon initial segment of motor axons we wondered whether similar distribution can be found in sensory axons. For this we expressed *flp* in multidendritic sensory neurons using the *pickpocket* Gal4 driver (*ppk-Gal4*). This allows labeling of the v'ada neurons (Figure 4A). Low levels of Para protein localize to the cell body and the distal shaft of the axon. Along the descending axon, Para localization increases only in some distance to the soma (Figure 4A,B,C). However, *para* expression in sensory neurons is not as strong as in motor axons which may correspond to the notion that sensory axons are usually smaller axons. The relatively low expression levels did not allow super-resolution imaging and thus, we could not address whether Para is found in a clustered organization along axons of *ppk* positive sensory neurons. Interestingly, however, within some of the v'ada dendrites, Para accumulates in distinct clusters (Figure 4A',B' arrows).

In conclusion, the above data show the presence of an axon initial segment in Drosophila motor and sensory axons. In motor axons, where this domain likely serves as a spike initiation zone (Günay et al., 2015), Para channels are organized in a clustered arrangement.

Electron microscopic analysis of Para cluster formation

To determine the distribution of Para on the subcellular level, we integrated an Apex2 encoding exon in the *para* locus, which allows generating local osmiophilic diaminobenzidine (DAB) precipitates that are detectable in the electron microscope (Lam et al., 2015). The insertion of an Apex2 encoding exon in the N-terminus of Para affected *para* function less strongly than the insertion of a *mCherry* exon and resulted in a very weak hypomorphic *para* allele (Figure 1A,B). In adult flies, $Para^{Apex2}$ is expressed in sufficient intensity to be detected along axons using the electron microscope. In small diameter peripheral axonal segments, weak $Para^{Apex2}$ directed DAB precipitates are found (Figure 5A, white arrowheads). In contrast, in large diameter axons next to the CNS/PNS boundary intense DAB precipitates can be detected (Figure 5B). When we performed serial sectioning the intensity of DAB labelling varied (Figure 5B-D), possibly reflecting the clustered localization of Para that we had found using the confocal microscope. We next determined the distribution of DAB precipitates along the circumference of an axon over 16 consecutive cross sections (Figure 5E,F). The resulting surface plot shows $Para^{Apex2}$ localization of a small segment of the axon in a 3D space. This suggests that $Para^{Apex2}$ clusters are organized in two lines along the ≈ 2.4 µm axonal circumference (Figure 5F,G), resembling the distribution of $Para^{mCherry}$ clusters along lines as detected using super-resolution light microscopy (Figure 3F). To further address the spacing of $Para^{Apex2}$ clusters along the longitudinal axis of the axon, we performed longitudinal sections of Para-rich axon segments and determined the staining intensity along the plasma membrane by using Fiji (Figure 5H,I). Here, again a spatial modulation of the Para staining intensity is apparent, with a spacing of

188 0.706 µm (Figure 5I; see Figure 3G for quantification, n=54 cluster distances on 6 axons), which
189 is similar to what we determined by confocal microscopy.

190

191 **Para-rich axon segments are embedded in a lacunar system formed by tract glia**

192 Interestingly, the large caliber axons decorated with highest levels of Para protein are
193 embedded in a mesh-like glial organization, that resembles the lacunar system described earlier
194 for the cockroach (Figure 5B-D, Figure 6A,B) (Wigglesworth, 1960). The Drosophila glial lacunar
195 system is characterized by intensive formation of glial processes around axons which are always
196 larger than 0.5 µm in diameter (Figure 6A,B, asterisks). Glial cell processes have an average
197 thickness of 35 nm (Figure 6A,B, n=189 processes, 4 nerves from 3 animals).

198 Next, we determined which glial cell type forms these lacunar structures. In the larva, the
199 central ensheathing/wrapping glial cells express the *83E12-Gal4* driver (Peco et al., 2016;
200 Pogodalla et al., 2021), whereas the peripheral wrapping glial cells can be addressed using the
201 *nrv2-Gal4 90C03-Gal80* driver (Kottmeier *et al.*, 2020; Matzat *et al.*, 2015; Stork *et al.*, 2008)
202 (Figure 1-figure supplement 1A,B). In adults – but not in larvae – a specialized group of glial cells
203 is found at the CNS/PNS boundary, called tract glia (Kremer et al., 2017) which overlaps with
204 both the central ensheathing glia and the peripheral wrapping glia (Figure 6-figure supplement
205 1). Interestingly, a similarly distinct group of glial cells has been identified in the vertebrate
206 nervous system (Fontenas and Kucenas, 2017; Kucenas et al., 2008; Kucenas et al., 2009). The
207 position of the lacunae coincides with the location of the tract glial cells (Kremer *et al.*, 2017)
208 (compare Figures 2H, 6C). These glial cells express *75H03-Gal4*, *83E12-Gal4* as well as the *nrv2-*
209 *Gal4 90C03-Gal80* driver (Figure 6-figure supplement 1). Multicolor flipout (MCFO2) labeling

experiments (Nern et al., 2015) indicate tiling of these glial cells along the nerve with no overlap and no spaces in between individual glial cells (Figure 6D-F). To further determine which glial cell forms the lacunar structures we generated flies harboring a *UAS-Myr-Flag-Apex2-NES* transgene (Apex2^{Myr}, see Materials and Methods) and expressed the myristoylated Apex2 with the different Gal4 drivers mentioned above. These experiments confirmed, that most of the lacunar system is indeed generated by tract glial cell processes (Figure 6A,B).

Thus, in large caliber motor axons, most of the Para voltage-gated sodium channels is positioned close to the lacunar system, which had been previously speculated to serve as an extracellular ion reservoir needed for sustained generation of action potentials (Chandra and Singh, 1983; Leech and Swales, 1987; Maddrell and Treherne, 1967; Treherne and Schofield, 1981; Van Harreveld et al., 1969; Wigglesworth, 1960).

Myelin in the leg nerve is found close to the CNS

In vertebrates, clustering of voltage-gated ion channels occurs on the edges of myelinated axonal segments (internodes) (Arancibia-Cárcamo *et al.*, 2017; Castelfranco and Hartline, 2015; Cohen *et al.*, 2019; Dutta *et al.*, 2018; Eshed-Eisenbach and Peles, 2019). Here, myelin not only participates in positioning of voltage-gated ion channels but also increases electric insulation and thus contributes to a faster conductance velocity. In Drosophila highest conductance velocity is likely to be required during fast and well-tuned locomotion in adults. Thus, we focused our search for myelin-like structures on adult leg nerves. Most of the 760 axons within an adult leg run in a single large nerve that exit the CNS at well-defined positions (Figure 7A-C-

figure supplement 1A,). Unlike the organization in larval nerves, axons running in the leg nerves are found in distinct zones depending on their diameter (Figure 7B,C). At the position of the femur, large axons are always covered by a single glial sheet. Small diameter axons are generally not individually wrapped but rather engulfed as a fascicle (Figure 7B,D). At the coxa, close to the CNS, we noted that large diameter axons were occasionally flanked by several glial membrane sheets (Figure 7E, asterisk). Up to 15 flat glial membrane sheets with a thickness of about 28 nm are found along larger axons (Figure 7E,F-figure supplement 1B). Axons with an intermediate diameter show individual glial wrapping with a single or very few glial sheets (Figure 7E,H). To quantify the occurrence of myelin-like structures we made semi-serial distal to proximal sections of six nerves every 5 µm across the entire lacunar area spanning 40 - 60 µm (Figure 7-figure supplement 2). The position where lacunar structures were first identified was set as zero. We then counted the occurrence of myelin-like structures in every section that we defined as ≥ 4 glial layers in close apposition. Here, we noted an increase in the number of myelin-like structures at the distal end of the lacunae (Figure 7-figure supplement 2B, Figure 7-figure supplement 3). No myelin-like structures were found at proximal positions close to the neuropil. The position of the up to 4 myelin-like structures found within a section plane was variable and could be either at the margin of the lacunae (Figure 7-figure supplement 3A) or could be found separating an area with small axons from an area with large axons (Figure 7-figure supplement 3B), or close to the blood-brain barrier (Figure 7-figure supplement 3C). In rare cases we noted formation of myelin-like membrane stacks without contact to axons in the lacunar region (Figure 7-figure supplement 3D). Myelin-like sheets contact serval axons (Figure

7-figure supplement 3A-C,E,F) but can also engulf single large axons with varying complexity of the membrane stacks (Figure 7-figure supplement 3G-H, Figure 7-figure supplement 4).

Myelin can be formed by central tract glia and peripheral wrapping glia

To determine which glial cell type is able to form myelin-like structures, we expressed Apex2^{Myr} in specific glial cell types and analyzed whether DAB positive myelin-like stacks of glial cell processes can be detected in the electron microscope. Upon expression of Apex2^{Myr} in CNS derived tract glia *75H03-Gal4* DAB positive myelin stacks can be detected (Figure 7G (black arrowhead),I, Figure 7-figure supplement 3, Figure 7-figure supplement 5). The finding that *75H03-Gal4* directed Apex2-labeling can be found next to unlabeled glial sheets (Figure 7G white arrowhead) suggests that peripheral wrapping glial cells can also form myelin-like structures in the leg nerve. Drosophila myelin-like membrane stacks are generated by extensive membrane folding providing the disadvantage that axons are not entirely insulated (Figure 7I, Figures S4, S5). However, we occasionally do find axons encircled by multiple glial wraps (Figure 7H, Figures S4,S5,S6). Interestingly, in some areas we noted almost compacted glial membrane sheets (Figure 7F,I, inlay boxed areas).

To further validate these findings we performed additional high pressure freezing of pre-fixed samples to optimize tissue preservation (Möbius et al., 2016; Sosinsky et al., 2008). In such specimens compact stackings of thin glial membrane sheets can be detected, too (Figure 7J,K). In the compacted areas (Figure 7I-K), the interperiodic distance of the different glial layers is about 30 nm, which is considerably more than the interperiodic distance of 13 nm found in mouse peripheral myelin (Fledrich et al., 2018). The unique compact appearance of vertebrate

myelin is mediated by the myelin basic protein (MBP) (Nave and Werner, 2021). In contrast to vertebrate myelin where extra- and intercellular space is removed, fly myelin-like structures only show an irregular compaction of the extracellular space.

Para localization depends on wrapping glial cells

Next, we wanted to test whether wrapping glial cells participate in the control positioning of voltage-gated ion channels. To address this, we ablated either peripheral wrapping glia or central ensheathing glia including the tract glia by directing the expression of the proapoptotic gene *hid* (Kottmeier *et al.*, 2020; Pogodalla *et al.*, 2021) and assayed the distribution of Shal and Para. Ablation of central or peripheral wrapping glial cells does not affect the distribution of the voltage-gated potassium channel Shal (Figure 8-figure supplement 1). Likewise, removal of the CNS specific ensheathing glia does not affect Para localization in the larval nervous system (Figure 8-figure supplement 2A-E). In contrast, upon ablation of the peripheral wrapping glia a marked change in Para protein localization becomes obvious (Figure 8-figure supplement 2A-B'). In control larvae, anti-Para antibodies detect only a weak labeling of segmental nerves, but all nerves are intensely decorated with Para in wrapping glia ablated larvae. Whereas in wild type control larvae, 2.5 times more Para protein is found at the CNS/PNS transition zone compared to nerve segments on the muscle field, an almost even distribution is noted in glia ablated larvae (Figure 8C). In addition to the redistribution of Para protein along the axon, we also noted a two-fold increase of *para* mRNA levels in further qRT-PCR experiments (Figure 8D).

Taken together, even in the small insect *Drosophila melanogaster*, myelin-like structures are formed (Figure 9). They are preferentially found distally to a lacunar region. The lacunae are formed by glial cell processes and comprise a large extracellular liquid filled space (Figure 9). Para voltage-gated sodium channels are differentially localized along sensory and motor neurons. In sensory neurons, Para expression is generally weaker and concentrates in an axon initial segment but is also found in dendritic processes. In motor neurons Para localization is enriched in axonal segments that are running within the glial lacunar system. Interestingly, glia ablation experiments indicate that normal *para* mRNA expression as well as Para protein localization is dependent on the presence of wrapping glial cell processes. This suggests a signaling pathway from glia to the regulation of *para* transcription.

Discussion

In the vertebrate nervous system, saltatory conductance allows very fast spreading of information. This requires localized distribution of voltage-gated ion channels and concomitantly, the formation of the myelin sheath. The evolution of this complex structure is unclear. Here, we report glial-dependent localization of voltage-gated ion channels at an AIS-like domain of peripheral Drosophila larval motor axons. As more channels accumulate in adults, a lacunar system and adjacent myelin-like structures are formed by central tract glia and peripheral wrapping glia.

In myelinated axons of vertebrates, voltage-gated Na^+ and K^+ channels are clustered at the AIS and the nodes of Ranvier (Amor et al., 2014; Freeman *et al.*, 2016; Nelson and Jenkins, 2017). In

315 invertebrate neurons, the AIS corresponds to the spike initiation zone located distal to the
316 soma and distal to the dendrite branching point. Such segments were found in C. elegans
317 (Eichel et al., 2022) and have been previously postulated for Drosophila neurons due to the
318 localization of a giant ankyrin, which in all systems appears to be an important scaffolding
319 protein at the AIS, as well as the presence of voltage-gated ion channels (Dubessy et al., 2019;
320 Freeman et al., 2015; Jegla et al., 2016; Ravenscroft *et al.*, 2020; Trunova et al., 2011).
321 Moreover, recent modeling approaches at the example of the pioneering aCC motor neuron
322 predicted the localization of voltage-gated ion channels at the CNS/PNS boundary (Günay *et al.*,
323 2015), which very well matches the localization of the voltage-gated ion channels Para and Shal,
324 as reported here. Interestingly, in Drosophila *para* mRNA expression as well as Para protein
325 localization depend on the presence of peripheral wrapping glia. In glia ablated nerves, Para
326 expression is increased and decorates the entire axonal membrane. This loss of a clustered
327 distribution may contribute to the pronounced reduction in axonal conductance velocity noted
328 earlier in such glia ablated animals (Kottmeier *et al.*, 2020). In addition, we found an increased
329 *para* mRNA expression. How glial cells control Para localization and how this is then transduced
330 to an increased expression of *para* remains to be further studied. Since alterations in glial
331 differentiation caused by manipulation of FGF-receptor signaling specifically in peripheral
332 wrapping glia does not cause a change in Para expression or localization (Figure 8-figure
333 supplement 2F-H), proteins secreted by wrapping glia might be needed for the correct
334 positioning of voltage-gated ion channels (Yuan and Ganetzky, 1999).

335 In the adult nervous system, the AIS-like domain is embedded in glial lacunar regions formed by
336 wrapping glial cell processes. The increased expression of Para within the AIS-like segments of

337 adult brains is expected to generate strong ephaptic coupling forces (Rey et al., 2022; Rey et al.,
338 2020). These are caused by ion flux through open channels which generate an electric field that
339 is able to influence the gating of ion channels in closely neighboring axons (Arvanitaki, 1942;
340 Krnjevic, 1986; Rasminsky, 1980). Ephaptic coupling helps to synchronize firing axons
341 (Anastassiou and Koch, 2015; Anastassiou et al., 2011; Han et al., 2018; Shneider and Pekker,
342 2015), but is also detrimental to the precision of neuronal signaling in closely apposed axons
343 (Arvanitaki, 1942; Kottmeier *et al.*, 2020).

344 Ephaptic coupling is counteracted by the glial lacunar system, that spatially separates axons and
345 adds more levels of wrapping. Furthermore, it was postulated that the lacunar system provides
346 a large extracellular ion reservoir (Wigglesworth, 1960). Given the tight apposition of axonal
347 and glial membranes with most parts of the nerve, which is in the range of 20 nm, only a very
348 small interstitial fluid volume is normally present. Thus, action potential generation would
349 deplete sodium and potassium ions very fast, and would prevent sustained neuronal activity.
350 The development of lacunar structures might therefore provide sufficient amount of ion and at
351 the same time physically separates axons to reduce the likelihood of ephaptic coupling. It will
352 be interesting to test this hypothesis in the future.

353 Close to the lacunar structures we detected myelin-like structures. It appears that the glial
354 processes that form the lacunae collapse to form compact myelin-like membrane sheets.
355 Interestingly, myelin-like structures are not formed at the lateral borders of the lacunae but
356 rather form at its distal end. This indicates that insulation is likely not a key function of the
357 myelin-like structures, but rather these structures originate as a consequence of the collapsed

lacunar system. Concomitant with the occurrence of the myelin-like differentiations we note a decrease in the Para ion channel density. At the same time, the need for a large ion reservoir decreases, favoring the formation of myelin-like structures.

A hallmark of vertebrate myelin is the spiral growth of the insulating glial membrane. This is generally not observed in large fly nerves where glial membrane sheets rather fold back than spirally grow around a single axon. Compared to myelinated vertebrate axons, this provides the disadvantage that axons are not entirely insulated. However, spiral growth can be seen in small nerves where less extensive wrapping is noted. An additional unique feature of vertebrate myelin is its compact organization which is mediated by the myelin basic protein (MBP) (Nave and Werner, 2021). In contrast to vertebrate myelin where extra- and intercellular space is removed, fly myelin-like structures only show a compaction of the extracellular space, which is expected to increase resistance as the number of freely moving ions is diminished. A fully compact myelin state would require MBP-like proteins which have not been identified in the fly genome.

In conclusion, the evolution of myelin appears reflected in the different developmental stages of Drosophila. First, voltage gated ion channels are clustered at the AIS with the help of Drosophila glia. Second, upon increased expression of such ion channels in the adult nervous system, an ion reservoir might be formed by the lacunar system. The collapse of glial processes in the non-lacunar regions then provides the basis of myelin formation. In the future, it will be interesting to identify glial derived signals that ensure channel positioning and determine how neuronal signaling adjusts channel expression and triggers formation of myelin.

379

Materials

Methods

Drosophila genetics

All fly stocks were raised and kept at room temperature on standard Drosophila food. All crosses were raised at 25 °C.

To determine temperature sensitivity, five 3-days old male and female flies were transferred to an empty vial with a foam plug. The vials were incubated in a water bath at 42°C for 1 min and then placed at room temperature. Flies were monitored every 15 secs for 5 min. At least 100 males and females for each genotype were tested.

For MCFO experiments early, white pupae were collected, put in a fresh vial and heat shocked at 37 °C for 1 hour. Pupae were placed back to 25 °C and dissected a few days after hatching.

To generate *para*^{mCherry} flies we employed the MiMIC insertion strain *para*^{Mi8578} generated by the Bellen lab and we injected pBS-KS-attB1-2-PT-SA-SD-0-mCherry (DGRC Stock 1299 ; https://dgrc.bio.indiana.edu//stock/1299 ; RRID:DGRC_1299 (Venken *et al.*, 2011)) into embryos with the following genotype: *y w* ***Φ****31*/*para*^{Mi08578}. Following crosses to *FM7c*, *y w* flies were tested by PCR to identify successful insertion events.

To generate *para*^{Apex2} flies, we first removed mCherry encoding sequences from pBS-KS-attB1-2-PT-SA-SD-0-mCherry (DGRC#1299) using restriction enzymes and then inserted the *apex2* coding sequence (addgene #49386, using the primers AAGGATCCGGAAAGTCTTACCCAACTGT

and AAGGATCCGGCATCAGCAAACCCAAG). pBS-KS-attB1-2-PT-SA-SD-0-Apex2 was used to establish a *para*^{Apex2} as described above. Flies were tested via single-fly PCR. To generate UAS-Myr-Flag-Apex2 flies we cloned Apex2 using the primers CACCgactacaaggatgacgacgataa and cagggtcaggcgctcc into pUAST_Myr_rfA_attB, which was then inserted into the landing stie 86Fb using established protocols (Bischof et al., 2007).

Western blot analysis

10 adult fly heads were homogenized in 50 µl RIPA buffer on ice. They were centrifuged at 4°C for 20 min at 13.000 rpm. The supernatant was mixed with 5x reducing Lämmli buffer and incubated for 5 min at 65°C. 15 µl of the samples were separated to an 8% SDS-gel and subsequently blotted onto a PVDF membrane (Amersham Hybond-P PVDF Membrane, GE Healthcare). Anti-Para antibodies were generated against the following N-terminal sequence (CAEHEKQKELERKRAEGE), affinity purified, and were used in a 1/1,000 dilution. Experiments were repeated three times.

Cell culture

Primary neural cell culture was preformed as described (Prokop et al., 2012). In brief, 3-5 stage11 embryos were collected, chemically dechorionized and homogenized in 100 µl dispersion medium. Following sedimentation for 5 min at 600 g, cells were resuspended in 30 µl culture medium and applied to a glass bottom chamber (MatTek), sealed with a ConA coated coverslip. Cultures were grown for 5-7 days. Experiments were repeated three times.

qPCR

RNA was isolated from dissected larval brains using the RNeasy mini kit (Qiagen) and cDNA was synthesised using Quantitect Reverse Transcription Kit (Qiagen) according to manufacturer's instructions. qPCR for all samples was performed using a Taqman gene expression assay (Life technologies) in a StepOne Real-Time PCR System (Thermofisher, para: Dm01813740_m1, RPL32: Dm02151827_g1). RPL32 was used as a housekeeping gene. Expression levels of Para were normalized to RPL32.

Immunohistochemistry

Larval Filets: L3 wandering larvae were collected in PBS on ice. Larvae were placed on a silicon pad and attached with two needles at both ends, with the dorsal side facing up. They were cut with a fine scissor at the posterior end. Following opening with a long cut from the posterior to the anterior end the tissue was stretched and attached to the silicon pad with additional 4-6 needles. Gut, fat body and trachea were removed. Adult brains: Adult flies were anesthetised with CO_2 and were dipped into 70% ethanol. The head capsule was cut open with fine scissors and the tissue surrounding the brain removed with forceps. Legs and wings were cut off and the thorax opened at the dorsal side. The ventral nerve cord was carefully freed from the tissue. For fixation, dissected samples were either covered for 3 min with Bouin's solution or for 20 min with 4% PFA in PBS. Following washing with PBT samples were incubated for 1 h in 10% goat serum in PBT. Primary antibody incubation was at 4°C followed. The following antibodies were used: anti-Para N-term, this study; anti-dsRed (Takara), anti-GFP (Abcam, Invitrogen), anti-Rumpel (Yildirim et al., 2022), anti-Repo (Hybridoma bank), rabbit α-V5 (1:500, Sigma Aldrich),

mouse α-HA (1:1000, Covance), rat α-Flag (1:200, Novus biologicals). The appropriate secondary antibodies (Thermofisher) were incubated for 3 hrs at RT. The tissues were covered with Vectashield mounting solution (Vector Laboratories) and stored at 4°C until imaging using a LSM880 Airyscan microscope, or a Elyra 7 microscope (Carl Zeiss AG Elyra 7 imaging, lateral resolution 80 nm with a voxel size of 30 nm x 30 nm x 100 nm). All stainings were repeated >5 times.

High Pressure Freezing

3 weeks old female flies were used with head, legs and tip of abdomen removed. Following fixation in 4% FA in 0.1M PHEM in a mild vacuum (-200 mbar), at RT for 45 min and 3 washes in 0.1 PHEM, the tissue was embedded in 3% low melting agarose for vibratome sectioning (Leica, VTS1200S). Samples were cut in PBS into 200 µm thick cross sections with 1mm/sec, 1.25mm amplitude. and were placed into lecithin coated 6 mm planchettes, filled with 20% PVP in 0.1M PHEM and high pressure frozen (Leica, HPM100). 7 specimens were sectioned. Freeze substitution was performed in 1 %OsO_4, 0.2%glutaraldehyde, 3% water in acetone at -90°C and stepwise dehydrated over 3days. Samples were embedded in mixtures of acetone and epon.

DAB Staining and electron microscopy

Flies were injected with 4% formaldehyde (FA) in 0.1 M HEPES buffer and fixed at room temperature for 45 min. Following washes and incubation in 20 mM glycine in 0.1 M HEPES, samples were incubated in 0.05 % DAB in 0.1 M HEPES at room temperature for 40 min. 0.03% H_2O_2 was added and the reaction was stopped after 5-10 min. The tissue was then fixed in 4%

FA and 0.2% glutardialdehyde in 0.1 M HEPES at RT for 3 h. After 3 times rinsing the tissue was fixed in 4% FA at room temperature overnight. The FA was replaced by 2% OsO_4 in 0.1 M HEPES for 1 h on ice (dark). Uranyl acetate staining was performed *en bloque* using a 2% solution in H_2O for 30 min (dark). Following an EtOH series (50%, 70%, 80%, 90% and 96%) on ice for 3 min each step, final dehydration was done at room temperature with 2x 100 % EtOH for 15 min and 2 times propylene oxide for 30 min. Grids of high pressure frozen samples were additionally counterstained with uranyl acetate and lead citrate. Following slow Epon infiltration specimens were embedded in flat molds and polymerized at 60 °C for 2 days.

6 specimens from 3 different fixation experiments were sectioned. Ultrathin sections were cut using a 35° ultra knife (Diatome) and collected in formvar coated one slot copper grids. For imaging a Zeiss TEM 900 at 80 kV in combination with a Morada camera (EMSIS, Münster, Germany) operated by the software iTEM. Image processing was done using Adobe Photoshop and Fiji. Ultrathin sections of high pressure frozen samples were examined at a Tecnai 12 biotwin (Thermo Fisher Scientific) and imaged with a 2K CCD veleta camera (EMSIS, Münster, Germany).

To plot the Para distribution across the axonal surface, an axon was serially sectioned (≈70 nm section thickness) and imaged. The images were cropped to the size of the axon in Fiji and aligned using Affinity Photo (software version 1.10.5.1342). The rotated / aligned images were loaded into Fiji and the segmented line tool was used to create ROIs on top of the axonal membrane in every section. The ROI was set to have the same starting point for the measurement. $Para^{Apex2}$ staining intensity was measured along the circumference of an axon on 16 sequentially sectioned EM images. The relative grey values were binned by a factor of 100.

This was then interpolated in 3D. We used biharmonic spline interpolation from the MATLAB Curve Fitting Toolbox (software version 9.13.0.2105380 (R2022b) Update 2) to generate a surface plot.

Script:

```
x=ParaE(:,1);
y=ParaE(:,3);
z=ParaE(:,2);
xlin = linspace(min(x), max(x), 100);
ylin = linspace(min(y), max(y), 100);
[X,Y] = meshgrid(xlin, ylin);
% Z = griddata(x,y,z,X,Y,'natural');
% Z = griddata(x,y,z,X,Y,'cubic');
Z = griddata(x,y,z,X,Y,'v4');
mesh(X,Y,Z)
axis tight; hold on
plot3(x,y,z,'.','MarkerSize',15)
```

Acknowledgements: We are grateful to all our colleagues for many discussions and P. Deing, K. Krukkert, K. Mildner and E. Naffin for excellent technical assistance. T. Zobel for help using the Elyra 7 microscope. B. Zalc and K.A. Nave for critical reading of the manuscript and many thoughtful suggestions. This work was supported by the Deutsche Forschungsgemeinschaft through funds to C.K. (SFB 1348, B5, Kl 588 / 29).

Competing interests: The authors declare that they have no competing interests.

Data and materials availability: All imaging and source data are available through: https://doi.org/10.57860/min_prj_000008.

All Drosophila strains reported are available upon request to C.K..

References

Allen, M.J., Godenschwege, T.A., Tanouye, M.A., and Phelan, P. (2006). Making an escape: development and function of the Drosophila giant fibre system. Semin Cell Dev Biol *17*, 31-41. 10.1016/j.semcdb.2005.11.011.

Amor, V., Feinberg, K., Eshed-Eisenbach, Y., Vainshtein, A., Frechter, S., Grumet, M., Rosenbluth, J., and Peles, E. (2014). Long-term maintenance of Na+ channels at nodes of Ranvier depends on glial contact mediated by gliomedin and NrCAM. Journal of Neuroscience *34*, 5089-5098. 10.1523/JNEUROSCI.4752-13.2014.

Anastassiou, C.A., and Koch, C. (2015). Ephaptic coupling to endogenous electric field activity: why bother? Current Opinion in Neurobiology *31*, 95-103. 10.1016/j.conb.2014.09.002.

Anastassiou, C.A., Perin, R., Markram, H., and Koch, C. (2011). Ephaptic coupling of cortical neurons. Nature Neuroscience *14*, 217-223. 10.1038/nn.2727.

Arancibia-Cárcamo, I.L., Ford, M.C., Cossell, L., Ishida, K., Tohyama, K., and Attwell, D. (2017). Node of Ranvier length as a potential regulator of myelinated axon conduction speed. eLife *6*. 10.7554/eLife.23329.

Arvanitaki, A. (1942). Effects evoked in an axon by the activity of a contiguous one. Journal of Neurophysiology *5*, 89-108. 10.1152/jn.1942.5.issue-2;requestedJournal:journal:jn;pageGroup:string:Publication.

Bischof, J., Maeda, R.K., Hediger, M., Karch, F., and Basler, K. (2007). An optimized transgenesis system for Drosophila using germ-line-specific phiC31 integrases. Proceedings of the National Academy of Sciences of the United States of America *104*, 3312-3317. 10.1073/pnas.0611511104.

Bittern, J., Pogodalla, N., Ohm, H., Bruser, L., Kottmeier, R., Schirmeier, S., and Klambt, C. (2021). Neuron-glia interaction in the Drosophila nervous system. Developmental Neurobiology *81*, 438-452. 10.1002/dneu.22737.

Castelfranco, A.M., and Hartline, D.K. (2015). The evolution of vertebrate and invertebrate myelin: a theoretical computational study. J Comput Neurosci *38*, 521-538. 10.1007/s10827-015-0552-x.

Chandra, P., and Singh, Y.N. (1983). Role of the perineurium and glial lacunar system in nutrition and storage of nutrients in the central nervous system of Spodoptera litura Fabr. (Lepidoptera: Noctulidae) at the time of reorganisation of the neural lamella during metamorphosis. Folia Histochem Cytochem (Krakow) *21*, 59-65.

Coggeshall, R.E., and Fawcett, D.W. (1964). The fine structure of the central nervous system of the leech, Hirudo medicinalis. Journal of Neurophysiology *27*, 229-289.

Cohen, C.C.H., Popovic, M.A., Klooster, J., Weil, M.-T., Möbius, W., Nave, K.-A., and Kole, M.H.P. (2019). Saltatory Conduction along Myelinated Axons Involves a Periaxonal Nanocircuit. Cell. 10.1016/j.cell.2019.11.039.

Davis, A.D., Weatherby, T.M., Hartline, D.K., and Lenz, P.H. (1999). Myelin-like sheaths in copepod axons. Nature *398*, 571. 10.1038/19212.

Dubessy, A.L., Mazuir, E., Rappeneau, Q., Ou, S., Abi Ghanem, C., Piquand, K., Aigrot, M.S., Thétiot, M., Desmazières, A., Chan, E., et al. (2019). Role of a Contactin multi-molecular complex secreted by oligodendrocytes in nodal protein clustering in the CNS. Glia *67*, 2248-2263. 10.1002/glia.23681.

566 Dutta, D.J., Woo, D.H., Lee, P.R., Pajevic, S., Bukalo, O., Huffman, W.C., Wake, H., Basser, P.J.,
567 SheikhBahaei, S., Lazarevic, V., et al. (2018). Regulation of myelin structure and conduction
568 velocity by perinodal astrocytes. Proceedings of the National Academy of Sciences *115*, 11832-
569 11837. 10.1073/pnas.1811013115.
570 Eichel, K., Uenaka, T., Belapurkar, V., Lu, R., Cheng, S., Pak, J.S., Taylor, C.A., Südhof, T.C.,
571 Malenka, R., Wernig, M., et al. (2022). Endocytosis in the axon initial segment maintains
572 neuronal polarity. Nature *609*, 128-135. 10.1038/s41586-022-05074-5.
573 Eshed-Eisenbach, Y., and Peles, E. (2019). The clustering of voltage-gated sodium channels in
574 various excitable membranes. Developmental Neurobiology. 10.1002/dneu.22728.
575 Fendl, S., Vieira, R.M., and Borst, A. (2020). Conditional protein tagging methods reveal highly
576 specific subcellular distribution of ion channels in motion-sensing neurons. eLife *9*.
577 10.7554/eLife.62953.
578 Fledrich, R., Abdelaal, T., Rasch, L., Bansal, V., Schütza, V., Brügger, B., Lüchtenborg, C., Prukop,
579 T., Stenzel, J., Rahman, R.U., et al. (2018). Targeting myelin lipid metabolism as a potential
580 therapeutic strategy in a model of CMT1A neuropathy. Nat Commun *9*, 3025. 10.1038/s41467-
581 018-05420-0.
582 Fontenas, L., and Kucenas, S. (2017). Livin' On The Edge: glia shape nervous system transition
583 zones. Curr Opin Neurobiol *47*, 44-51. 10.1016/j.conb.2017.09.008.
584 Freeman, S.A., Desmazières, A., Fricker, D., Lubetzki, C., and Sol-Foulon, N. (2016). Mechanisms
585 of sodium channel clustering and its influence on axonal impulse conduction. Cellular and
586 molecular life sciences : CMLS *73*, 723-735. 10.1007/s00018-015-2081-1.

Freeman, S.A., Desmazières, A., Simonnet, J., Gatta, M., Pfeiffer, F., Aigrot, M.S., Rappeneau, Q., Guerreiro, S., Michel, P.P., Yanagawa, Y., et al. (2015). Acceleration of conduction velocity linked to clustering of nodal components precedes myelination. Proceedings of the National Academy of Sciences *112*, E321-328. 10.1073/pnas.1419099112.

Gisselbrecht, S., Skeath, J.B., Doe, C.Q., and Michelson, A.M. (1996). heartless encodes a fibroblast growth factor receptor (DFR1/DFGF-R2) involved in the directional migration of early mesodermal cells in the Drosophila embryo. Genes & Development *10*, 3003-3017.

Günay, C., Sieling, F.H., Dharmar, L., Lin, W.H., Wolfram, V., Marley, R., Baines, R.A., and Prinz, A.A. (2015). Distal spike initiation zone location estimation by morphological simulation of ionic current filtering demonstrated in a novel model of an identified Drosophila motoneuron. PLoS Comput Biol *11*, e1004189. 10.1371/journal.pcbi.1004189.

Günther, J. (1976). Impulse conduction in the myelinated giant fibers of the earthworm. Structure and function of the dorsal nodes in the median giant fiber. The Journal of Comparative Neurology *168*, 505-531. 10.1002/cne.901680405.

Hama, K. (1959). Some observations on the fine structure of the giant nerve fibers of the earthworm, Eisenia foetida. The Journal of Biophysical and Biochemical Cytology *6*, 61-66. 10.1083/jcb.6.1.61.

Hama, K. (1966). The fine structure of the Schwann cell sheath of the nerve fiber in the shrimp (Penaeus japonicus). J Cell Biol *31*, 624-632. 10.1083/jcb.31.3.624.

Han, K.S., Guo, C., Chen, C.H., Witter, L., Osorno, T., and Regehr, W.G. (2018). Ephaptic Coupling Promotes Synchronous Firing of Cerebellar Purkinje Cells. Neuron *100*, 564-578.e563. 10.1016/j.neuron.2018.09.018.

609 Hartline, D.K., and Colman, D.R. (2007). Rapid conduction and the evolution of giant axons and
610 myelinated fibers. Current biology *17*, R29-35. 10.1016/j.cub.2006.11.042.
611 Herzmann, S., Krumkamp, R., Rode, S., Kintrup, C., and Rumpf, S. (2017). PAR-1 promotes
612 microtubule breakdown during dendrite pruning in Drosophila. The EMBO journal *36*, 1981-
613 1991. 10.15252/embj.201695890.
614 Hess, A. (1958). The fine structure and morphological organization of the peripheral nerve-
615 fibres and trunke of the cockroach (Periplaneta americana). Quarterly Journal of Microscopical
616 Science *99*, 333-340. 10.1152/jn.1964.27.2.229.
617 Heuser, J.E., and Doggenweiler, C.F. (1966). The fine structural organization of nerve fibers,
618 sheaths, and glial cells in the prawn, Palaemonetes vulgaris. J Cell Biol *30*, 381-403.
619 10.1083/jcb.30.2.381.
620 Hodgkin, A.L., and Huxley, A.F. (1952). A quantitative description of membrane current and its
621 application to conduction and excitation in nerve. The Journal of physiology *117*, 500-544.
622 10.1016/j.devcel.2018.10.002.
623 Igaki, T., Kanuka, H., Inohara, N., Sawamoto, K., Núñez, G., Okano, H., and Miura, M. (2000).
624 Drob-1, a Drosophila member of the Bcl-2/CED-9 family that promotes cell death. Proc Natl
625 Acad Sci U S A *97*, 662-667. 10.1073/pnas.97.2.662.
626 Jegla, T., Nguyen, M.M., Feng, C., Goetschius, D.J., Luna, E., van Rossum, D.B., Kamel, B.,
627 Pisupati, A., Milner, E.S., and Rolls, M.M. (2016). Bilaterian Giant Ankyrins Have a Common
628 Evolutionary Origin and Play a Conserved Role in Patterning the Axon Initial Segment. PLoS
629 Genetics *12*, e1006457. 10.1371/journal.pgen.1006457.

Jenett, A., Rubin, G.M., Ngo, T.-T.B., Shepherd, D., Murphy, C., Dionne, H., Pfeiffer, B.D., Cavallaro, A., Hall, D., Jeter, J., et al. (2012). A GAL4-driver line resource for Drosophila neurobiology. Cell reports *2*, 991-1001. 10.1016/j.celrep.2012.09.011.

Kottmeier, R., Bittern, J., Schoofs, A., Scheiwe, F., Matzat, T., Pankratz, M., and Klämbt, C. (2020). Wrapping glia regulates neuronal signaling speed and precision in the peripheral nervous system of Drosophila. Nature communications *11*, 4491-4417. 10.1038/s41467-020-18291-1.

Kremer, M.C., Jung, C., Batelli, S., Rubin, G.M., and Gaul, U. (2017). The glia of the adult Drosophila nervous system. Glia *65*, 606-638. 10.1002/glia.23115.

Krnjevic, K. (1986). Ephaptic Interactions: A Significant mode of Communications in the Brain. Physiology (Bethesda, Md.) *1*, 28-29. 10.1152/physiologyonline.1986.1.1.28.

Kroll, J.R., Saras, A., and Tanouye, M.A. (2015). Drosophila sodium channel mutations: Contributions to seizure-susceptibility. Experimental neurology *274*, 80-87. 10.1016/j.expneurol.2015.06.018.

Kucenas, S., Takada, N., Park, H.-C., Woodruff, E., Broadie, K., and Appel, B. (2008). CNS-derived glia ensheath peripheral nerves and mediate motor root development. Nature Neuroscience *11*, 143-151. 10.1038/nn2025.

Kucenas, S., Wang, W.D., Knapik, E.W., and Appel, B. (2009). A selective glial barrier at motor axon exit points prevents oligodendrocyte migration from the spinal cord. J Neurosci *29*, 15187-15194. 10.1523/jneurosci.4193-09.2009.

650 Lam, S.S., Martell, J.D., Kamer, K.J., Deerinck, T.J., Ellisman, M.H., Mootha, V.K., and Ting, A.Y.
651 (2015). Directed evolution of APEX2 for electron microscopy and proximity labeling. Nature
652 Methods *12*, 51-54. 10.1038/nmeth.3179.
653 Leech, C.A., and Swales, L.S. (1987). Enzyme effects on the connective tissues of an insect
654 central nervous system. Tissue Cell *19*, 587-598. 10.1016/0040-8166(87)90050-4.
655 Levi, J.U., Cowden, R.R., and Collins, G.H. (1966). The microscopic anatomy and ultrastructure of
656 the nervous system in the earthworm (Lumbricus sp.) with emphasis on the relationship
657 between glial cells and neurons. J Comp Neurol *127*, 489-510. 10.1002/cne.901270405.
658 Maddrell, S.H., and Treherne, J.E. (1967). The ultrastructure of the perineurium in two insect
659 species, Carausius morosus and Periplaneta americana. Journal of Cell Science *2*, 119-128.
660 Mahr, A., and Aberle, H. (2006). The expression pattern of the Drosophila vesicular glutamate
661 transporter: a marker protein for motoneurons and glutamatergic centers in the brain. Gene
662 expression patterns : GEP *6*, 299-309. 10.1016/j.modgep.2005.07.006.
663 Matzat, T., Sieglitz, F., Kottmeier, R., Babatz, F., Engelen, D., and Klämbt, C. (2015). Axonal
664 wrapping in the Drosophila PNS is controlled by glia-derived neuregulin homolog Vein.
665 Development *142*, 1336-1345. 10.1242/dev.116616.
666 Möbius, W., Nave, K.-A., and Werner, H.B. (2016). Electron microscopy of myelin: Structure
667 preservation by high-pressure freezing. Brain research *1641*, 92-100.
668 10.1016/j.brainres.2016.02.027.
669 Moran, Y., Barzilai, M.G., Liebeskind, B.J., and Zakon, H.H. (2015). Evolution of voltage-gated ion
670 channels at the emergence of Metazoa. Journal of Experimental Biology *218*, 515-525.
671 10.1242/jeb.110270.

672 Nave, K.-A., and Werner, H.B. (2014). Myelination of the nervous system: mechanisms and
673 functions. Annual Review of Cell and Developmental Biology *30*, 503-533. 10.1146/annurev-
674 cellbio-100913-013101.
675 Nave, K.-A., and Werner, H.B. (2021). Ensheathment and Myelination of Axons: Evolution of
676 Glial Functions. Annual Review of Neuroscience *44*, 197-219. 10.1146/annurev-neuro-100120-
677 122621.
678 Nelson, A.D., and Jenkins, P.M. (2017). Axonal Membranes and Their Domains: Assembly and
679 Function of the Axon Initial Segment and Node of Ranvier. Frontiers in Cellular Neuroscience
680 *11*, 136. 10.3389/fncel.2017.00136.
681 Nern, A., Pfeiffer, B.D., and Rubin, G.M. (2015). Optimized tools for multicolor stochastic
682 labeling reveal diverse stereotyped cell arrangements in the fly visual system. Proceedings of
683 the National Academy of Sciences of the United States of America *112*, E2967-E2976.
684 10.1073/pnas.1506763112.
685 Peco, E., Davla, S., Camp, D., M Stacey, S., Landgraf, M., and van Meyel, D.J. (2016). Drosophila
686 astrocytes cover specific territories of the CNS neuropil and are instructed to differentiate by
687 Prospero, a key effector of Notch. Development *143*, 1170-1181. 10.1242/dev.133165.
688 Pérez-Moreno, J.J., and O'Kane, C.J. (2019). GAL4 Drivers Specific for Type Ib and Type Is Motor
689 Neurons in Drosophila. G3 (Bethesda, Md.) *9*, 453-462. 10.1534/g3.118.200809.
690 Pogodalla, N., Kranenburg, H., Rey, S., Rodrigues, S., Cardona, A., and Klämbt, C. (2021).
691 Drosophila ßHeavy-Spectrin is required in polarized ensheathing glia that form a diffusion-
692 barrier around the neuropil. Nature communications *12*, 6357-6318. 10.1038/s41467-021-
693 26462-x.

694 Prokop, A., Küppers-Munther, B., and Sánchez-Soriano, N. (2012). Using Primary Neuron
695 Cultures of Drosophila to Analyze Neuronal Circuit Formation and Function. In The Making and
696 Un-Making of Neuronal Circuits in Drosophila, B.A. Hassan, ed. (Humana Press), pp. 225-247.
697 10.1007/978-1-61779-830-6_10.
698 R Caré, B., Emeriau, P.-E., Cortini, R., Victor, J.-M., and France;, S.U.U.U.P.U.L.F.-P. (2015).
699 Chromatin epigenomic domain folding: size matters. AIMS Biophysics *2*, 517-530.
700 10.3934/biophy.2015.4.517.
701 Rasminsky, M. (1980). Ephaptic transmission between single nerve fibres in the spinal nerve
702 roots of dystrophic mice. The Journal of Physiology *305*, 151-169.
703 10.1113/jphysiol.1980.sp013356.
704 Ravenscroft, T.A., Janssens, J., Lee, P.-T., Tepe, B., Marcogliese, P.C., Makhzami, S., Holmes, T.C.,
705 Aerts, S., and Bellen, H.J. (2020). Drosophila Voltage-Gated Sodium Channels Are Only
706 Expressed in Active Neurons and Are Localized to Distal Axonal Initial Segment-like Domains.
707 Journal of Neuroscience *40*, 7999-8024. 10.1523/JNEUROSCI.0142-20.2020.
708 Rey, S., Ohm, H., and Klämbt, C. (2022). Axonal ion homeostasis and glial differentiation. FEBS J.
709 10.1111/febs.16594.
710 Rey, S., Zalc, B., and Klämbt, C. (2020). Evolution of glial wrapping: A new hypothesis.
711 Developmental Neurobiology *81*, 453-463. 10.1002/dneu.22739.
712 Roots, B.I. (2008). The phylogeny of invertebrates and the evolution of myelin. Neuron glia
713 biology *4*, 101-109. 10.1017/S1740925X0900012X.
714 Roots, B.I., and Lane, N.J. (1983). Myelinating glia of earthworm giant axons: thermally induced
715 intramembranous changes. Tissue & Cell *15*, 695-709.

716 Salvaterra, P.M., and Kitamoto, T. (2001). Drosophila cholinergic neurons and processes
717 visualized with Gal4/UAS-GFP. Brain research. Gene expression patterns *1*, 73-82.
718 10.1016/S1567-133X(01)00011-4.
719 Shneider, M.N., and Pekker, M. (2015). Correlation of action potentials in adjacent neurons. -
720 PubMed - NCBI. Physical Biology *12*, 066009.
721 Sosinsky, G.E., Crum, J., Jones, Y.Z., Lanman, J., Smarr, B., Terada, M., Martone, M.E., Deerinck,
722 T.J., Johnson, J.E., and Ellisman, M.H. (2008). The combination of chemical fixation procedures
723 with high pressure freezing and freeze substitution preserves highly labile tissue ultrastructure
724 for electron tomography applications. J Struct Biol *161*, 359-371. 10.1016/j.jsb.2007.09.002.
725 Stork, T., Engelen, D., Krudewig, A., Silies, M., Bainton, R.J., and Klämbt, C. (2008). Organization
726 and function of the blood-brain barrier in Drosophila. Journal of Neuroscience *28*, 587-597.
727 10.1523/JNEUROSCI.4367-07.2008.
728 Sun, B., Xu, P., and Salvaterra, P.M. (1999). Dynamic visualization of nervous system in live
729 Drosophila. Proceedings of the National Academy of Sciences of the United States of America
730 *96*, 10438-10443. 10.1073/pnas.96.18.10438.
731 Treherne, J.E., and Schofield, P.K. (1981). Mechanisms of ionic homeostasis in the central
732 nervous system of an insect. J Exp Biol *95*, 61-73. 10.1242/jeb.95.1.61.
733 Trunova, S., Baek, B., and Giniger, E. (2011). Cdk5 regulates the size of an axon initial segment-
734 like compartment in mushroom body neurons of the Drosophila central brain. Journal of
735 Neuroscience *31*, 10451-10462. 10.1523/JNEUROSCI.0117-11.2011.

Van Harreveld, A., Khattab, F.I., and Steiner, J. (1969). Extracellular space in the central nervous system of the leech, Mooreobdella fervida. Journal of Neurobiology *1*, 23-40. 10.1002/neu.480010104.

Venken, K.J.T., Schulze, K.L., Haelterman, N.A., Pan, H., He, Y., Evans-Holm, M., Carlson, J.W., Levis, R.W., Spradling, A.C., Hoskins, R.A., and Bellen, H.J. (2011). MiMIC: a highly versatile transposon insertion resource for engineering Drosophila melanogaster genes. Nature Methods *8*, 737-743. 10.1038/nmeth.1662.

Wigglesworth, V.B. (1959). The Histology of the Nervous System of an Insect, Rhodnius prolixus. Quarterly Journal of Microscopical Science *100*, 299-313.

Wigglesworth, V.B. (1960). The Nutrition of the Central Nervous System in the Cockroach Periplaneta Americana L. The Role of Perineurium and Glial Cells in the Mobilization of Reserves. Journal of Experimental Biology *37*, 500-512. 10.1242/jeb.37.3.500.

Wilson, C.H., and Hartline, D.K. (2011a). The novel organization and development of copepod myelin. I. Ontogeny. The Journal of Comparative Neurology *519*, 3259-3280. 10.1002/cne.22695.

Wilson, C.H., and Hartline, D.K. (2011b). Novel organization and development of copepod myelin. ii. nonglial origin. The Journal of Comparative Neurology *519*, 3281-3305. 10.1002/cne.22699.

Yildirim, K., Winkler, B., Pogodalla, N., Mackensen, S., Baldenius, M., Garcia, L., Naffin, E., Rodrigues, S., and Klambt, C. (2022). Redundant functions of the SLC5A transporters Rumpel, Bumpel, and Kumpel in ensheathing glial cells. Biol Open *11*. 10.1242/bio.059128.

Yuan, L.L., and Ganetzky, B. (1999). A glial-neuronal signaling pathway revealed by mutations in a neurexin-related protein. Science *283*, 1343-1345.

Figures

Figure 1 Localization of Para voltage-gated ion channels in the larval nervous system.

(A) Schematic view on the *para* gene. Alternative splicing at the circled exons results in the generation of more than 60 Para isoforms. All isoforms share a common N-terminus. Here, the MiMIC insertion *MI08578* allows tagging of the endogenous *para* gene. The peptide sequence AEHEKQKELERKRAEGE (position 33-49) that was used for immunization is indicated by a green star, the MiMIC insertion is indicated by a magenta star. **(B)** Homozygous $para^{mCherry}$, $para^{Apex2}$ or $para^{ST76}$ flies were tested for temperature induced paralysis. The recovery time is indicated. **(C)** Third instar larval $para^{mCherry}$ nervous system stained for Cherry localization. $Para^{mCherry}$ is detected in the ventral nerve cord (vnc) and diffusely along peripheral nerves (arrows). **(D,D')** Affinity purified anti-Para antibodies detect a protein in the CNS of dissected 24 hours old wild type first instar larvae. **(E,E')** No protein is found in the CNS of dissected age-matched *para* mutant animals. **(F)** Third instar larval nervous system stained with the pre-immune control. **(G)** Third instar larval nervous system stained with affinity purified anti-Para antibodies. Scale bars are as indicated.

Figure 2 Differential localization of voltage-gated ion channels in Drosophila

(A) Third instar larvae with the genotype [$para^{mCherry}$; *OK371-Gal4, UAS-mCherry*^{dsRNA}]. $para^{mCherry}$ expression is suppressed in all glutamatergic neurons and thus, $Para^{mCherry}$ localization along axons of cholinergic sensory neurons becomes visible. **(B)** Third instar larvae with the genotype [$para^{mCherry}$; *Chat-Gal4, UAS-mCherry*^{dsRNA}]. Here expression of $para^{mCherry}$ is

suppressed in all cholinergic neurons which reveals Para localization in motor neurons. Note the prominent Para localization at the CNS/PNS transition point (arrowheads). **(C)** Third instar larval *shaker*^{GFP} nervous system stained for GFP localization. Shaker is found in the neuropil (dashed areas). **(D)** Third instar larval *shab*^{GFP} nervous system stained for GFP localization. Shab is distributed evenly along all peripheral axons. **(E)** Third instar larval *shal*^{GFP} nervous system stained for GFP localization. Shal localizes similar as Para on motor axons. Scale bars are 100 µm. **(F)** Adult *para*^{mCherry} ventral nerve cord stained for Para localization. Para^{mCherry} localizes prominently along segments of peripheral nerves (arrow) as they enter thoracic neuromeres. Note that some axons entering the CNS neuropil show only a weak Para signal (open arrowhead). **(G)** Control (*Oregon R*) adult ventral nerve cord stained for Para protein localization using purified anti-Para antibodies. Note the differential localization of Para along axons entering the nerve (arrow, open arrowhead). **(H)** Ventral nerve cord of an adult fly with the genotype [*para*$^{FlpTag\text{-}GFP}$*; Ok371-Gal4, UAS-flp*]. The boxed area is shown enlarged in **(H')**. The arrowheads point to high density of Para. **(I)** Ventral nerve cord of an adult fly with the genotype [*para*$^{FlpTag\text{-}GFP}$*; Chat-Gal4, UAS-flp*]. The boxed area is shown enlarged in **(H')**. Note, that Para localization is reduced as soon axons enter the neuropil (arrows). Scale bars are as indicated.

Figure 3 Clustered localization of Para along motor axons.

(A) High resolution Airyscan analysis of Para^{mCherry} and **(B)** HRP localization in an adult nerve. The boxed area is shown in higher magnification below (*A',B'*). Note the clustered appearance of Para^{mCherry}, clusters are about 0.6-0.8 µm apart (arrowheads). **(C,C')** Primary wild type neural

cells cultured for 7 days stained for Repo (magenta) to label glial nuclei, HRP (cyan) to label neuronal cell membranes and anti-Para antibodies (green). The Para protein localizes in a dotted fashion. **(D)** Ventral nerve cord of a third instar larva with the genotype [*para*$^{FlpTag\text{-}GFP}$*; 94G06-Gal4, UAS-flp*]. The arrow points to a single neuronal cell body found in every hemineuromer. **(E)** Higher magnification of single Para^{GFP} expressing axons. Note the dotted arrangement of Para^{GFP} along motor axons (arrowheads). **(F,F')** Ventral nerve cord of a third instar larva with the genotype [*para*$^{FlpTag\text{-}GFP}$*; 94G06-Gal4, UAS-flp*] imaged with super-resolution. The dashed box is shown in high magnification in **(F')**. Arrows point to clusters of Para protein. Scale bars are as indicated. **(G)** Quantification of Para cluster distance using super-resolution imaging (Para$^{FlpTag::GFP}$, average distance is 620 nm, n=91 clusters on 3 axons, 2 larvae) or electron microscopy (Para^{Apex2}, average distance is 706 nm, n=64 clusters on 8 axons 4 larvae, Mann-Whitney-U, p=0.0747, two-tailed). Scale bars are as indicated.

Figure 4 Localization of Para along sensory axons.

(A,A') Ventral *pickpocket* expressing sensory neuron (v'ada) of a third instar larva with the genotype [*para*$^{FlpTag\text{-}GFP}$*; ppk-Gal4, UAS-flp, UAS-tdTomato*] stained for GFP (green), HRP (magenta) and tdTomato (white). The dashed boxes are shown in higher magnification in (B,C). The asterisk denotes the position of the neuronal cell soma. The filled arrows indicate localized Para along some of the dendritic processes. The open arrowhead points to a dendritic process lacking Para localization. Note that Para localization along the descending axon becomes prominent only after about 50 µm (open arrow). **(B,B')** Magnification of the neuronal soma attached dendrites. **(C,C')** Descending axon of the v'ada neuron. Note that the strong Para

signal starts 50 µm distal to the cell soma and fades out after 100 µm (open arrows). Scale bars are as indicated.

Figure 5 A glial lacunar system surrounds the axon initial segment.

(**A)** Weak Para expression can be detected on *para*^{Apex2} expressing small axons (arrowheads) running in fascicles within the nerve. **(B-D)** Cross-sections through the same axon at various positions. Distance between individual sections (B,C) is 15 µm, distance between (C,D) is 6.5 µm. Note the intense labeling of the axonal membrane is changing between the different sections. **(E)** Cross section, to determine the staining intensity along the membrane (below the blue line), a corresponding ROI was defined and **(F)** quantified using Fiji. **(G)** Surface plot of Para^{Apex2} distribution along 16 consecutive axonal cross sections. For details see Materials and Methods. The intensity of DAB precipitates is transformed to different colors. Note that Para clusters are organized in two longitudinal lines across the axonal membrane surface. **(H)** Longitudinal section of a *para*^{Apex2} expressing axon. The staining intensity along the membrane (above the blue line) was quantified using Fiji. **(I)** Staining intensity of the membrane stretch shown in (H). Note the regular increase in staining intensity every 0.6-0.8 µm. For quantification see Figure 3G. Scale bars are as indicated.

Figure 6 Organization of the lacuna forming tract glial.

(A,B) Apex2 expression directed by *75H03-Gal4*. Axons (asterisks) are engulfed by lacunar structures that are largely formed by the tract glia. **(C)** Maximum projection of a confocal image

stack. *75H03-Gal4* directed expression of GFP labels the ensheathing/wrapping or tract glia. Note that GFP expression ends proximal to the dissection cut (white dashed circles). **(D-F)** MCFO2 analysis of the *nrv2-Gal4, R90C03-Gal80* positive wrapping glia. Note that glial cells tile the nerve roots with no gaps in between. Scale bars are as indicated.

Figure 7 Drosophila wrapping glia form myelin.

(A) Drosophila leg of a three weeks old fly with wrapping glial nuclei in green, the cuticle is stained by autofluorescence, the genotype is [*nrv2-Gal4, UAS-lamGFP*]. **(B-K)** Electron microscopic images of sections taken from 3 weeks old female flies. **(B)** Section at the level of the femur. **(C)** Electron microscopic section at the level of the coxa. In some areas, an increased amount of glial membranes can be detected close to large caliber axons (box with white dashed lines, enlarged as an inlay) . **(D,E,G)** Cross sections through a 2 weeks adult leg of a fly with the genotype [*75H03-Gal4, UAS-Myr-Flag-Apex2-NES*]. Glial cell processes are stained by the presence of Apex2 which generates an osmiophilic DAB precipitate. **(D)** Small caliber axons (ax) are engulfed by a single glial process as fascicle. Larger axons are individually wrapped (asterisk). **(E)** Large caliber axons are surrounded by glial membrane stacks. The asterisk denotes an axon engulfed by a few glial wraps (red dots). ax: axon. **(F)** Up to 15 densely packed membrane sheets are found (see inlay for enlargement). **(G)** Darkly stained tract glia membrane stacks (black arrowhead) can be found next to unlabeled membrane stacks (white arrowhead), suggesting that myelin-like structures can be derived from both, central and peripheral wrapping glial cells. **(H)** High pressure freezing preparation showing a single axon covered by myelin-like membrane sheets in a lacunar area (asterisks). **(I)** Note the bulged

appearance of the growing tip of the glial cell processes that form the myelin-like structures (arrowheads). The inlay shows a highly organized membrane stacking. **(J,K)** High pressure freezing preparation of prefixed samples to reduce tissue preparation artifacts. Note the compact formation of membrane layers. The white dashed area is shown in **(K)**. Scale bars are as indicated.

Figure 8 Localization of the voltage-gated sodium channel depends on glia.

(A,A') Third instar larval filet preparation with the genotype [*nrv2-Gal4, UAS-CD8-GFP; R90C03-Gal80*] showing the localization of Para as detected using the anti-Para antibody in a control larva. **(B,B')** Third instar larval filet preparation with the genotype [*nrv2-Gal4, UAS-hid; R90C03-Gal80*] showing the localization of Para as detected using the anti-Para antibody in a wrapping glia ablated larva. The white dashed boxes were used for quantification of Para fluorescence intensity in the CNS/PNS transition zone in relation to its expression in the muscle field area. The yellow boxed areas are shown in higher magnification (A',B'). Note the increased localization of Para along the peripheral nerve at the level of the muscle field (asterisks). Scale bars are as indicated. **(C)** Quantification of Para fluorescence intensity in the CNS/PNS transition area and the muscle field area in control and wrapping glia ablated larvae (n=10 larval filets, 3 nerves/filet). To exclude a possible influence seen in individual animals, the average fluorescence intensities along nerves of each individual were compared. Note, Para distributes more evenly along the axon in the absence of wrapping glia (p=0,0003; Mann-Whitney-U-test). **(D)** Quantification of *para* mRNA expression using qRT-PCR in control and wrapping glia ablated larvae (n=7, with 15-20 brains each). *para* ct-values were normalized to ct-values of control

gene, *RPL32*. Note, the significant increase in *para* mRNA expression upon wrapping glia ablation (p=0,0006, Mann-Whitney-U-test). Scale bars are as indicated.

Figure 9 Organization of the axon initial segment in Drosophila motor axons

Voltage-gated sodium channels are preferentially positioned at the axon initial segment (AIS) of the motor axon. **(A)** In the larval nervous system positioning is mediated by the peripheral wrapping glia. **(B)** In adults these cells form myelin-like structures, which fray out in the lacunae which represent a reservoir possibly needed for ion homeostasis during sustained action potential generation.

Supplementary Figures

Figure 1-figure supplement 1 (A-C) Schematic representation of the larval (A,B) and the adult Drosophila nervous system (C). The ensheathing glia is labelled in blue, the ensheathing/wrapping glia is labelled in green, the wrapping glia is shown in red. The tract glia of the adult nervous system is shown in green and red stripes. The tract glia likely corresponds to the ensheathing/wrapping glia but the exact lineage relationship is not known. **(D)** Western blot of protein lysates of adult heads. Purified anti-Para antibodies detect a band of 105 kDa and a band of >250 kDa in size. The size of the >250 kDa protein band increases in $para^{mCherry}$ heads compared to wild type control as well as $para^{MiMIC}$ heads, indicating that this band corresponds to the Para protein. Note that elevated levels of the endogenous Para::mCherry fusion protein are detected. Anti-dsRed antibodies detect only the $Para^{mCherry}$ fusion protein.

Figure 2-figure supplement 1 (A-C) The tract glial cells as defined by *75H03-Gal4 UAS-tdTomato* activity, also express the CNS ensheathing glia marker *83E12-LexA LexAop-CD8::GFP*. **(D)** The PNS wrapping glia marker *nrv2-Gal4 90C03-Gal80 UAS-mCherry* labels cells that overlap in their expression domain with the tract glial cells. HRP (blue) labels neuronal membranes. Scale bar is 100 µm. **(E)** Schematic summary of central and peripheral wrapping glial cells in Drosophila. The neuropil is covered by the ensheathing glia. The peripheral axons are wrapped by the peripheral wrapping glia. The *75H03-Gal4* positive glial cells are located in between these two glial cell populations.

Figure 7-figure supplement 1 (A) About 760 axons innervate the leg. The majority is smaller than 0.5 µm in diameter, very few ones are larger than 2 µm. **(B)** The width of glial cell processes is about 28 nm and very regular.

Figure 7-figure supplement 2 Extent of the lacunar system. **(A)** CNS/PNS boundary of the mesothoracic neuromere of an adult ventral nerve cord with the genotype [*75H03-Gal4, UAS-tdTomato, 83E12-lexA, lexAop-CD8GFP*] imaged for tdTomato, GFP and HRP expression. **(B)** Schematic representation of the image shown in (A) with the position of the lacunar region indicated. **(C-F)** Examples of a serial section series taken every 5 µm for 40 - 65 µm. The green shading indicates the lacunar region. The numbers in circles show relative distances to the first distal section with lacunar structures. Scale bars are as indicated.

Figure 7-figure supplement 3 Quantification of myelin distribution in the leg nerve. **(A-I)** Examples of myelin-like structures of the leg nerve. **(A)** Myelin-like sheets can be found separating the lacunar region from small caliber axons. **(B)** Myelin-like sheets separate large caliber axons from small caliber axons. **(C)** Myelin-like sheets can be found towards the blood-brain barrier. **(D)** Myelin-like sheets are rarely found in the lacunar region without close contact to axons. **(E,F)** Myelin-like sheets can partially wrap larger axons. **(G-I)** Myelin-like sheets can be found with different complexity around single large caliber axons. **(J)** Quantification of the number of myelin-like stacks detected in a specific section plane (see Figure S3). The value set as 0 corresponds to the distal most point where lacunar structures were detected. Progression

of sections is towards the CNS (proximal). **(K)** Quantification of the number of axons contacting the myelin-like stacks.

Figure 7-figure supplement 4 Multilayered myelin-like structures are formed around single axons in the adult nervous system. **(A)** Loosely wrapped glial membranes around one single axon (asterisk). The spacing of the glial membranes resembles the glial lacunae. **(B)** Wrapping around a single axon. The green shaded glial cell process wraps spirally around the central axon. The ends are denoted by the asterisk and the circle. **(C)** Simple wrapping around single axons. The shading indicates the different glial cell types present in the nerve: Wrapping glia WG, perineurial glia PG, subperineurial glia SPG. **(D)** Tight wrapping around a single axon. Unlike the image shown in (A) a close apposition of glial membranes is noted. Scale bars are as indicated.

Figure 7-figure supplement 5 Formation of myelin-like structures in the adult CNS of Drosophila. **(A)** High pressure freezing preparation. Spiral growth of a glial cell process. **(B)** Membrane stack formed by a wrapping glial cell. Note the bulbed growing tips of the glial membrane sheets (arrowheads). **(C-F)** Myelin-like membrane sheets can be connected by comb-like structures. (C) Overview of a multilayered membrane stack around several axons, red shading highlights some of the glial membrane sheets. The arrowhead indicates a bulb structure at the end of the glial membrane sheet (D). In some cases, the ends of the membrane sheets are connected by comb-like structures (asterisks) (E). Growing tip of a wrapping glial cell process that navigated around an axon (ax) (F). Scale bars are as indicated.

Figure 8-figure supplement 1 Glia ablation does not affect the localization of the voltage-gated potassium channel Shal. **(A)** Control larva with an endogenously tagged Shal potassium channel. Shal predominantly localizes to the axon initial segment. **(B)** Upon ablation of the ensheathing glia, no change in Shal localization is detected. **(C)** Control larva. The inlay shows co-staining for wrapping glial cell processes (magenta) and HRP to detect neuronal membranes. **(D)** Upon ablation of wrapping glia, no change in Shal localization is detected. Scale bars are as indicated.

Figure 8-figure supplement 2 Ablation of central ensheathing glia does not affect positioning of Para at the AIS. CNS preparations of third instar larvae of the genotypes indicated are shown. **(A)** Control larva, expressing CD8GFP under the control of the split Gal4 driver [*83E12-Gal4^{AD}, repo-Gal4^{DBD}, UAS-CD8GFP*] specific for ensheathing glial cells stained for Para protein expression. **(B)** Upon ablation of the ensheathing glia following expression of the proapoptotic gene *hid* no change in the Para expression levels are detected. **(C)** Quantification of the Para fluorescence intensity in control and ensheathing glia ablated larvae (n=5 larval brains, 10-16 nerves/brain). To exclude influence of individual animals 10-16 nerves per individual were measured and analysis was performed on the mean fluorescence intensity of all values from one animal (p=0,8016, Mann-Whitney-U-test). **(D)** Control larvae for ensheathing glia ablation using the FlpTag approach. The GFP encoding exon was flipped in all motor neurons using [*vGlut-lexA, lexAop-Flp*]. Note, the pronounced localization of Para^{GFP} at the AIS-like domain of the nerve. **(E)** Upon ablation of the ensheathing glial cells no change in Para localization in motor axons can be detected. **(F-H)** Filet preparations of third instar larvae stained for Para localization. Control larva (F). Upon expression of activated FGF-receptor Heartless no change in

Para localization is noted (G). Upon expression of dominant negative Heartless no change in Para localization is noted (H). Scale bars are as indicated.

Zip file Fiugre 1-figure supplement 1 with source data

Four images of western blots, with and without marker bands, are provided.

Key Resources Table				
Reagent type (species) or resource	**Designation**	**Source or reference**	**Identifiers**	**Additional information**
genetic reagent (*Drosophila melanogaster*)	*y[1] w[*] Mi{MIC}MI08578a Mi{MIC}MI08578b*	Bloomington Drosophila Stock Center	BDSC51087	
genetic reagent (*Drosophila melanogaster*)	*y[1] w[*] Mi{FlpStop}para[MI08578-FlpStop.D]/FM7c*	Bloomington Drosophila Stock Center	BDSC67680	
genetic reagent (*Drosophila melanogaster*)	*Para-mCherry*	This study		Figures 1, 2
genetic reagent (*Drosophila melanogaster*)	*Para-Apex*	This study		Figures 1, 5
genetic reagent (*Drosophila melanogaster*)	*Para-FlpTag GFP/Fm7i*	Fendl et al., 2020		
genetic reagent (*Drosophila melanogaster*)	*y[1] w[*]; Mi{PT-GFSTF.1}Shal[MI00446-GFSTF.1]*	Bloomington Drosophila Stock Center	BDSC60149	
genetic reagent (*Drosophila melanogaster*)	*y[1] w[*] Mi{PT-GFSTF.2}Sh[MI10885-GFSTF.2]/FM7j, B[1]*	Bloomington Drosophila Stock Center	BDSC59423	
genetic reagent (*Drosophila melanogaster*)	*y[1] w[*]; Mi{PT-GFSTF.1}Shab[MI00848-GFSTF.1]/TM6C, Sb[1] Tb[1]*	Bloomington Drosophila Stock Center	BDSC60514	
genetic reagent (*Drosophila melanogaster*)	*y[1] sc[*] v[1] sev[21]; P{y[+t7.7] v[+t1.8]=VALIUM20-mCherry}attP2*	Bloomington Drosophila Stock Center	BDSC35785	
genetic reagent (*Drosophila melanogaster*)	*UAS-CD8GFP II; R90C03Gal80 III*	Kottmeier et al., 2020		

genetic reagent (*Drosophila melanogaster*)	*UAS-Hid/CyOw; R90C03Gal80 III*	Kottmeier et al., 2020		
genetic reagent (*Drosophila melanogaster*)	*UAS-lacZ NLS II*	Y. Hirmoi		
genetic reagent (*Drosophila melanogaster*)	*UAS-lambda-Htl*	Gisselbrecht et al., 1996		
genetic reagent (*Drosophila melanogaster*)	*UAS-htl^{DN} II*	Bloomington Drosophila Stock Center	BDSC5366	
genetic reagent (*Drosophila melanogaster*)	*UAS-CD8GFP II*	Bloomington Drosophila Stock Center	BDSC5137	
genetic reagent (*Drosophila melanogaster*)	*UAS-CD8mCherry II*	Bloomington Drosophila Stock Center	BDSC 27391	
genetic reagent (*Drosophila melanogaster*)	*UAS-Hid II*	Igaki et al., 2000		
genetic reagent (*Drosophila melanogaster*)	*UAS-Flp*	Bloomington Drosophila Stock Center	BDSC 4539	
genetic reagent (*Drosophila melanogaster*)	*UAS-Myr-Flag-APEX2-NES^{86Fb} III*	This study		Figures 6, 7
genetic reagent (*Drosophila melanogaster*)	*pBPhsFLP2::pEST / I ; ; UAS HA, FLAG, V5, OLLAS / III*	Nern et al., 2015)		
genetic reagent (*Drosophila melanogaster*)	*ChAT-Gal4*	Salvaterra and Kitamoto, 2001		

genetic reagent (*Drosophila melanogaster*)	*OK371-Gal4*	Mahr and Aberle, 2006		
genetic reagent (*Drosophila melanogaster*)	*GMR94G06Gal4 III*	Bloomington Drosophila Stock Center	BDSC40701	
genetic reagent (*Drosophila melanogaster*)	*Nrv2Gal4 II*	Sun et al., 1999		
genetic reagent (*Drosophila melanogaster*)	*Nrv2Gal4 II; R90C03Gal80 III*	Kottmeier et al., 2020		
genetic reagent (*Drosophila melanogaster*)	*Nrv2Gal4 II; R90C03Gal80, UAS-CD8Cherry III*	Kottmeier et al., 2020		
genetic reagent (*Drosophila melanogaster*)	*GMR83E12_AD II; Repo4.3_DBD III*	Bittern et al., 2021		
genetic reagent (*Drosophila melanogaster*)	*GMR75H03-Gal4 III*	Bloomington Drosophila Stock Center	BDSC39908	
genetic reagent (*Drosophila melanogaster*)	*ppkGal4, AUS-tdTomato III*	Herzmann et al., 2017		
genetic reagent (*Drosophila melanogaster*)	*lexAop-Flp III*	Bloomington Drosophila Stock Center	BDSC55819	
genetic reagent (*Drosophila melanogaster*)	*w[*]; TI{2A-lexA::GAD}VGlut[2A-lexA]/CyO*	Bloomington Drosophila Stock Center	BDSC84442	
genetic reagent (*Drosophila melanogaster*)	$Para^{ST76}$	Bloomington Drosophila Stock Center	BDSC26701	

genetic reagent (*Drosophila melanogaster*)	*Oregon R*	Bloomington Drosophila Stock Center	BDSC5	
antibody	Anti-Para N-term (rabbit, polyclonal)	This study		IF (1:1000), WB (1:1000) Figures 1, 2,3
antibody	Anti-dsRed (rabbit, polyclonal)	Takara	Cat# 632496 RRID:AB_10013483	IF (1:1000)
antibody	Anti-GFP (chicken, polyclonal)	Abcam	Cat# ab13970 RRID:AB_300798	IF(1:500)
antibody	Anti-GFP (rabbit, polyclonal)	Invitrogen	Cat# **A-11122 RRID:AB_221569**	IF(1:1000)
antibody	Anti-Rumpel (rabbit, polyclonal)	Yildirim et al., 2022		IF(1:1000)
antibody	Anti-Repo (mouse, monoclonal)	Hybridoma bank	Cat# 8D12 RRID: AB_528448	IF(1:5)
antibody	Anti-V5 (rabbit, polyclonal)	Sigma-Aldrich	Cat# V8137-.2MG RRID:AB_261889	IF(1:500)
antibody	Anti-HA (mouse, monoclonal)	Covance BioLegend	Cat# MMS-101R RRID:AB_291262	IF(1:1000)
antibody	Anti-Flag (rat, monoclonal)	Novus biologicals	Cat# NBP1-06712SS RRID:AB_162598	IF(1:200)
antibody	FluoTag®-X4 anti-GFP (Alpaca, monoclonal)	NanoTag Biotechnologies	Cat# N0304 RRID:AB_2905516	IF(1:500)
antibody	FluoTag®-X4 anti-RFP (Alpaca, monoclonal)	NanoTag Biotechnologies	Cat# N0404 RRID:AB_2744638	IF(1:500)

antibody	Anti-rabbit Alexa 488 (goat, polyclonal)	Thermofisher	Cat # A-11008 RRID:AB_143165	IF(1:1000)
antibody	Anti-rabbit Alexa 568 (goat, polyclonal)	Thermofisher	Cat # A-11011 RRID:AB_143157	IF(1:1000)
antibody	Anti-chicken Alexa 488 (goat, polyclonal)	Thermofisher	Cat# A-11039, RRID:AB_2534096	IF(1:1000)
antibody	Anti-mouse Alexa 488 (goat, polyclonal)	Thermofisher	Cat# A-11001, RRID:AB_2534069	IF(1:1000)
antibody	Anti-HRP Alexa 647 (goat, polyclonal)	Thermofisher	Cat# 123-605-021, RRID:AB_2338967	IF(1:500)
antibody	Anti-rabbit HRP (goat, polyclonal)	Invitrogen	Cat # 31460 RRID:AB_228341	WB(1:5000)
recombinant DNA reagent	pBS-KS-attB1-2-PT-SA-SD-0-mCherry	Drosophila Genome Research Centre	DGRC#1299	
recombinant DNA reagent	pBS-KS-attB1-2-PT-SA-SD-0-Apex2	This study		Generation of transgenic fly
sequenced-based reagent	BamH1 Apex2 fwd	This study	PCR Primer	AAGGATCCGGAAAGTCTTACCCAACTGT
sequenced-based reagent	BamH1 Apex2 rev	This study	PCR Primer	AAGGATCCGGCATCAGCAAACCCAAG
sequenced-based reagent	MiLF	Venken et al., 2011	PCR Primer	GCGTAAGCTACCTTAATCTCAAGAAGAG
sequenced-based reagent	MiLR	Venken et al., 2011	PCR Primer	CGCGGCGTAATGTGATTTACTATCATAC
sequenced-based reagent	mCherry-Seq fwd		PCR Primer	ACGGCGAGTTCATCTACAAG

sequenced-based reagent	mCherry-Seq rev		PCR Primer	TTCAGCCTCTGCTTGATCTC
sequenced-based reagent	Apex253_rev1	This study	PCR Primer	AGCTCAAAATAGGGAACTCCG
sequenced-based reagent	Apex286_fwd1	This study	PCR Primer	TACCAGTTGGCTGGCGTTGTT
sequenced-based reagent	Para qPCR Primer	Thermofisher Scientific	Cat#4331182 Dm01813740_m1	
sequenced-based reagent	RPL32 qPCR Primer	Thermofisher Scientific	Cat#4331182 Dm02151827_g1	
commercial assay or kit	RNeasy Kit	Quiagen	Cat#74104	
commercial assay or kit	Quantitect Reverse Transcription Kit	Quiagen	Cat#205313	
commercial assay or kit	Taqman™ gene expression assay, Universal Master Mix II, with UNG	Thermofisher Scientific	Cat#4440038	
Software algorithm	GraphPad PRSIM	GraphPad Software, USA	Version 6.0	
Software algorithm	Fiji	https://imagej.net/software/fiji/		
Software algorithm	ZEN Software	Zeiss	Black version	
Software algorithm	Affinity Photo	Serif (Europe)		

Software algorithm	MatLab	The MathWorks, Inc.		
Software algorithm	Photoshop CS6	Adobe		

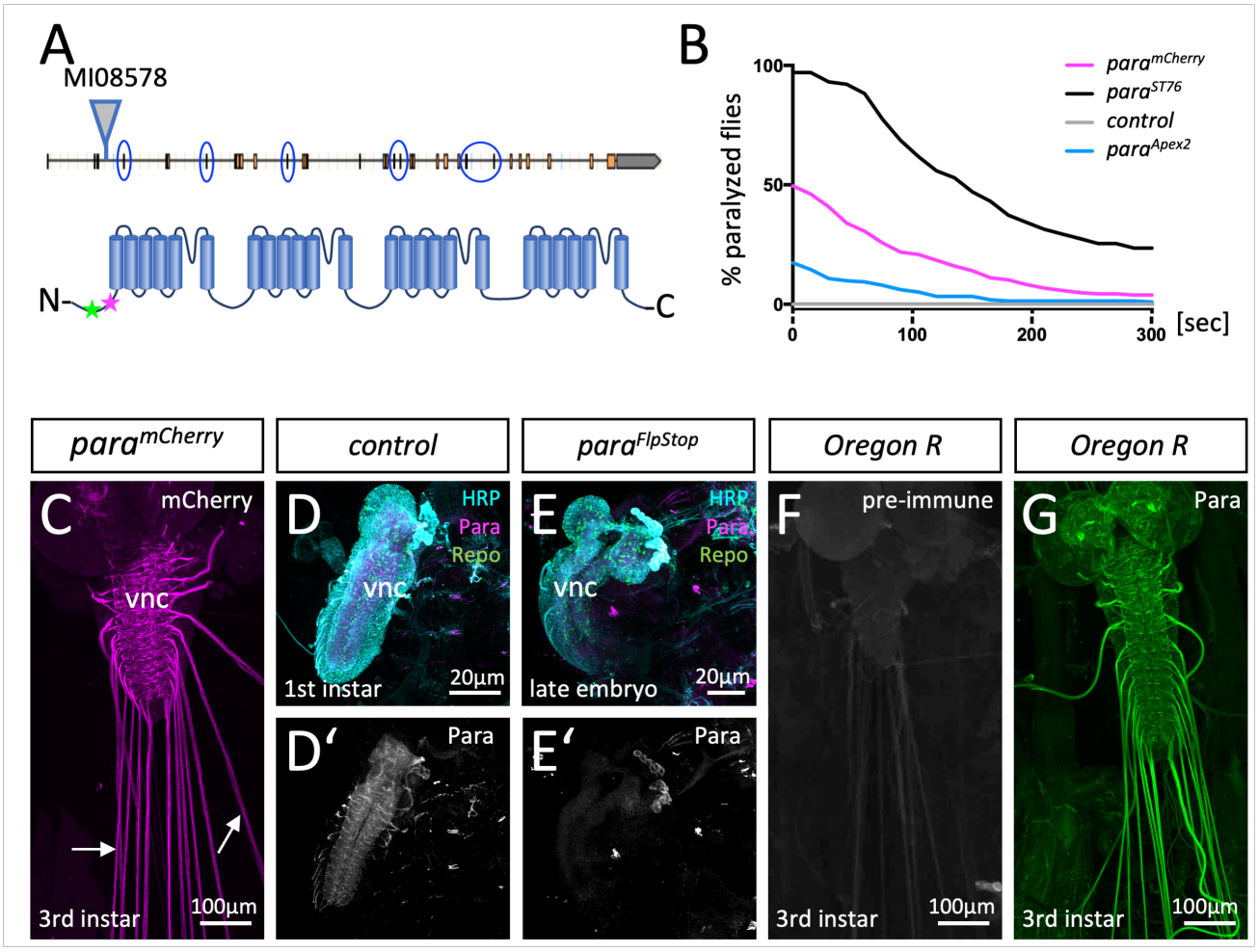
A
MI08578
N
C
B
100
50
0
% paralyzed flies
0
100
200
300
[sec]
para^mCherry
para^ST76
control
para^Apex2
para^mCherry
control
para^FlpStop
Oregon R
Oregon R
C
mCherry
vnc
3rd instar
100µm
D
HRP
Para
Repo
vnc
1st instar
20µm
D'
Para
E
HRP
Para
Repo
vnc
late embryo
20µm
E'
Para
F
pre-immune
3rd instar
100µm
G
Para
3rd instar
100µm

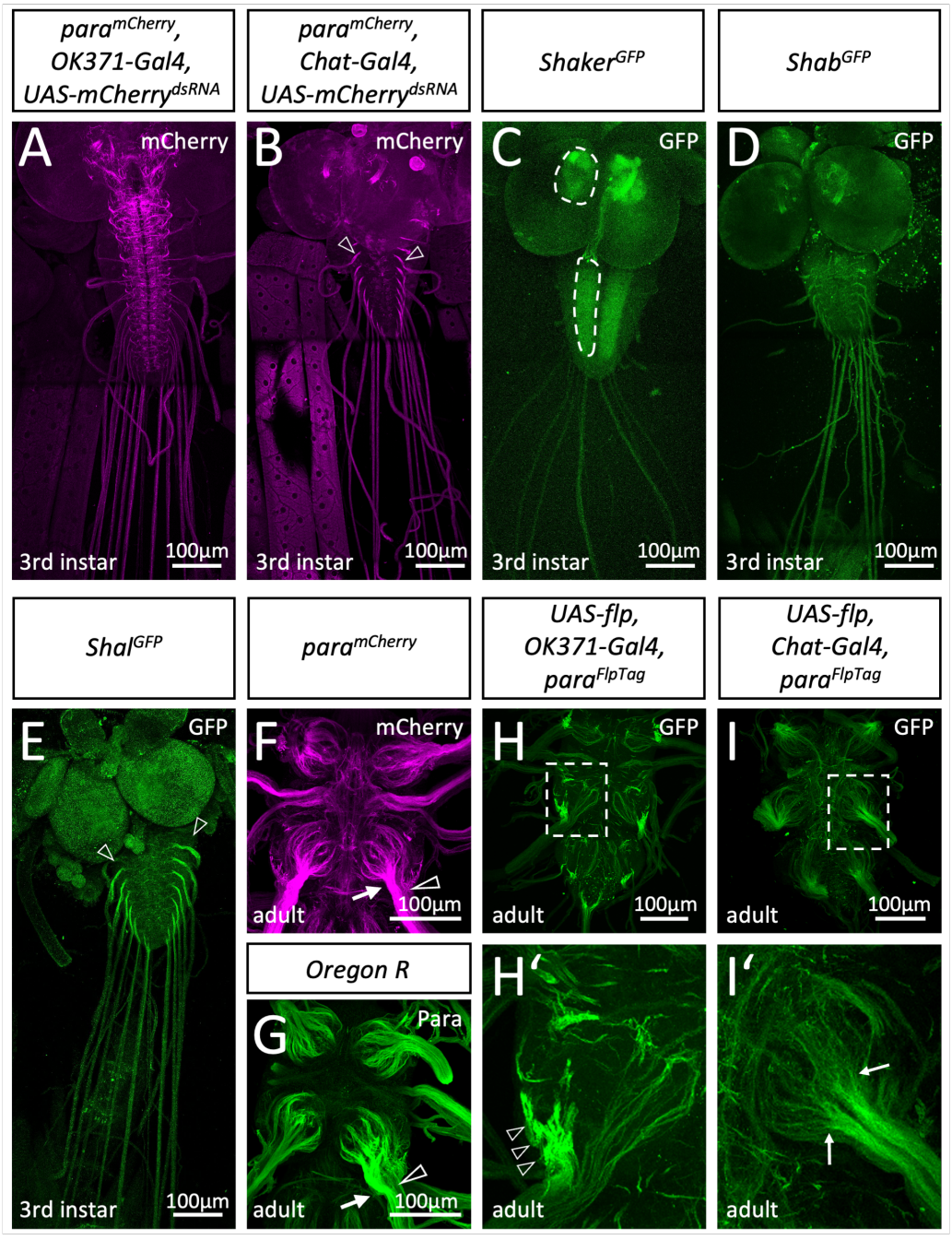
para^mCherry, OK371-Gal4, UAS-mCherry^dsRNA
para^mCherry, Chat-Gal4, UAS-mCherry^dsRNA
Shaker^GFP
Shab^GFP
A
mCherry
3rd instar
100µm
B
mCherry
3rd instar
100µm
C
GFP
3rd instar
100µm
D
GFP
3rd instar
100µm
Shal^GFP
para^mCherry
UAS-flp, OK371-Gal4, para^FlpTag
UAS-flp, Chat-Gal4, para^FlpTag
E
GFP
3rd instar
100µm
F
mCherry
adult
100µm
H
GFP
adult
100µm
I
GFP
adult
100µm
Oregon R
G
Para
adult
100µm
H'
adult
I'
adult

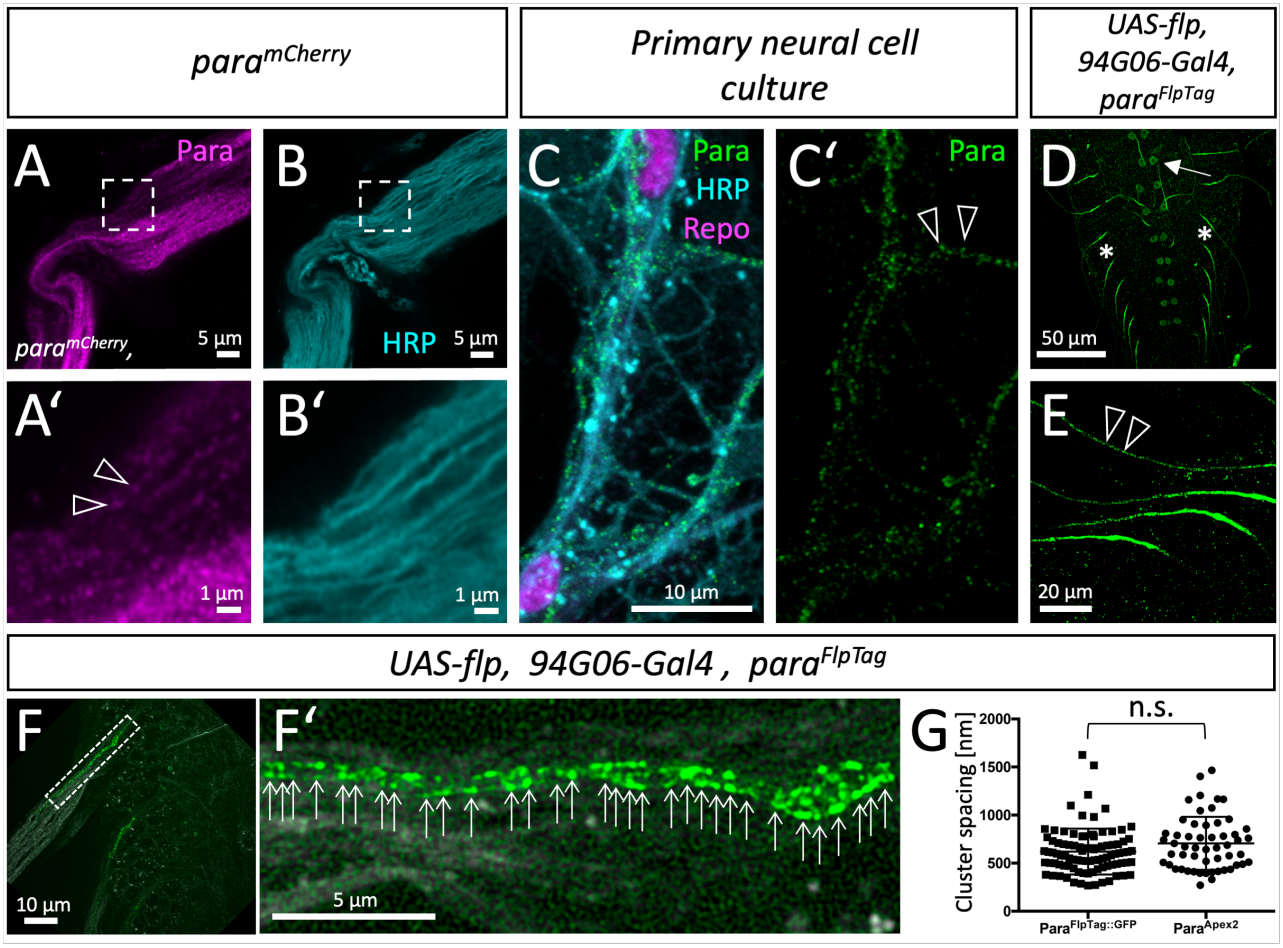
para^mCherry
Primary neural cell culture
UAS-flp, 94G06-Gal4, para^FlpTag
A
Para
para^mCherry,
5 µm
B
HRP
5 µm
C
Para
HRP
Repo
10 µm
C'
Para
D
50 µm
A'
1 µm
B'
1 µm
E
20 µm
UAS-flp, 94G06-Gal4 , para^FlpTag
F
10 µm
F'
5 µm
G
n.s.
Cluster spacing [nm]
2000
1500
1000
500
0
Para^FlpTag::GFP
Para^Apex2

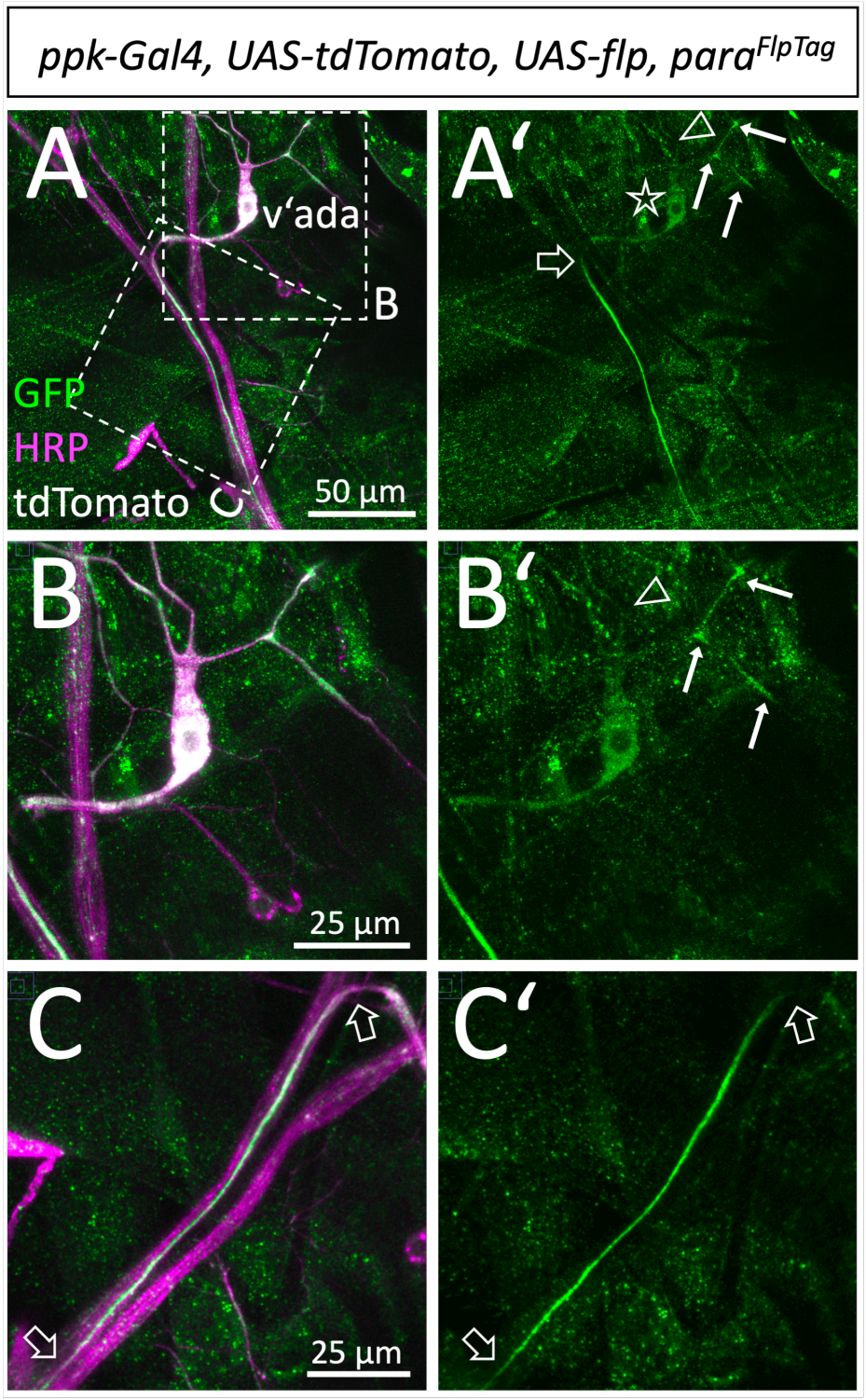
ppk-Gal4, UAS-tdTomato, UAS-flp, para^FlpTag
A
v'ada
B
GFP
HRP
tdTomato
50 µm
A'
B
25 µm
B'
C
25 µm
C'

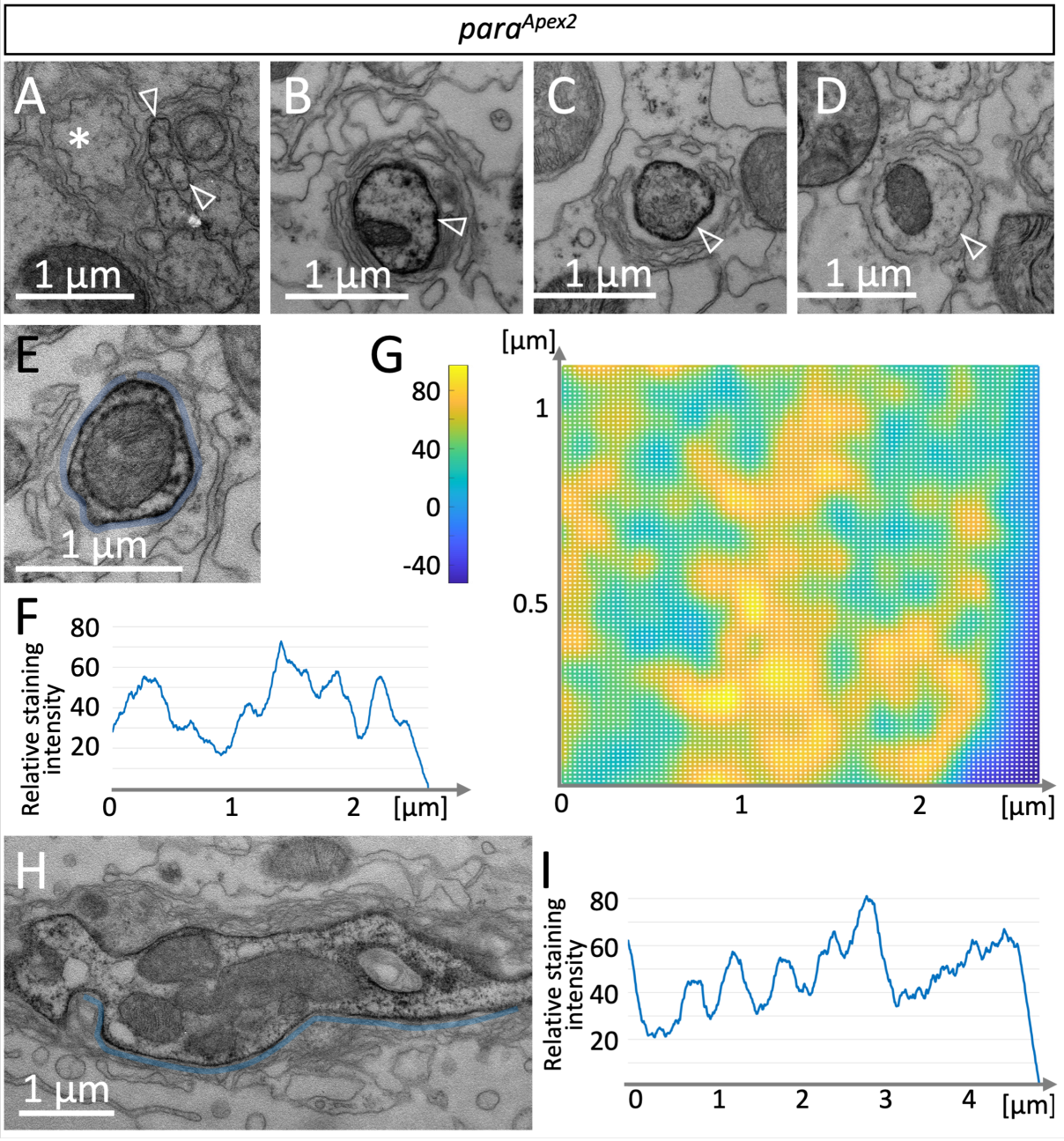
para^Apex2
A
B
C
D
1 µm
E
1 µm
G
80
40
0
-40
[µm]
1
0.5
0
1
2
[µm]
F
Relative staining intensity
80
60
40
20
0
1
2
[µm]
H
1 µm
I
Relative staining intensity
80
60
40
20
0
1
2
3
4
[µm]

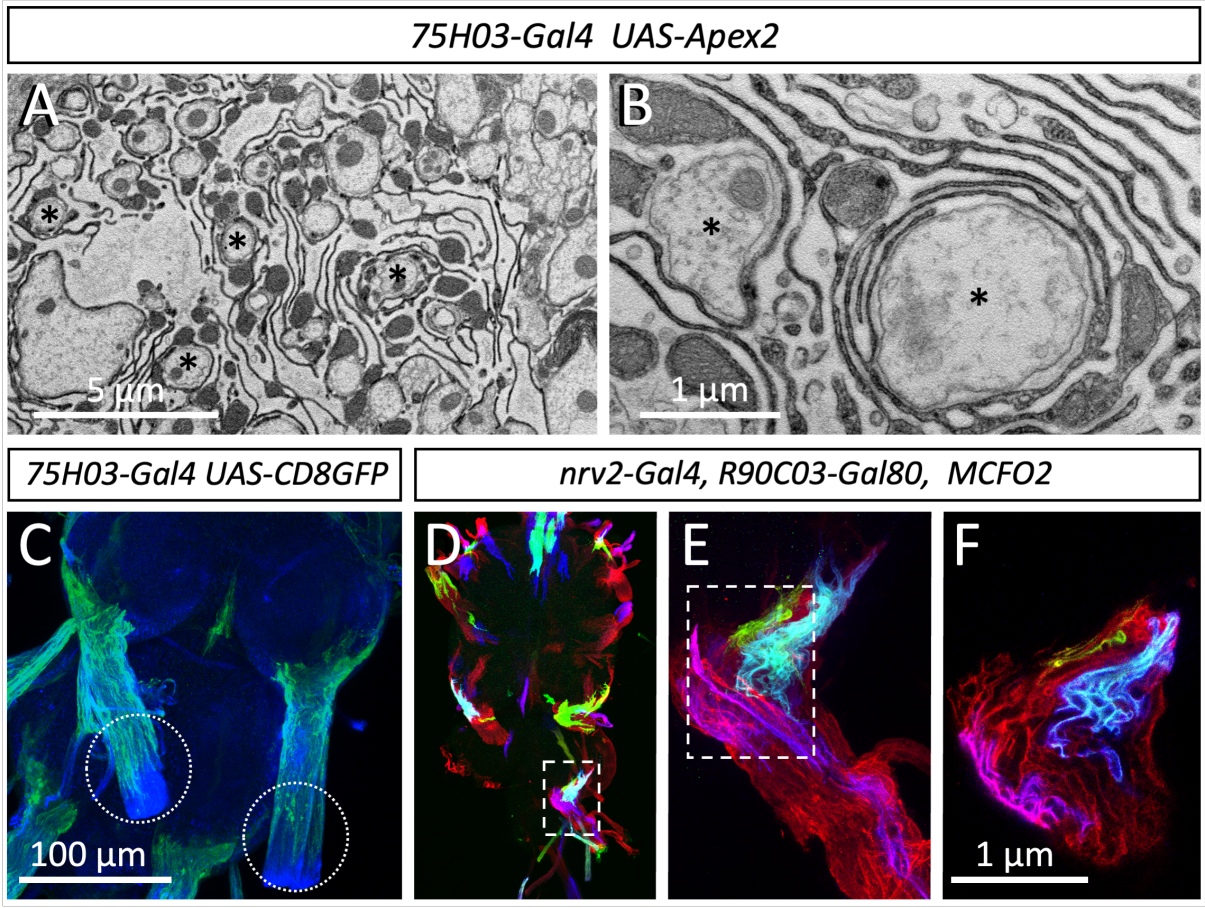
75H03-Gal4 UAS-Apex2
A
5 µm
B
1 µm
75H03-Gal4 UAS-CD8GFP
nrv2-Gal4, R90C03-Gal80, MCFO2
C
100 µm
D
E
F
1 µm

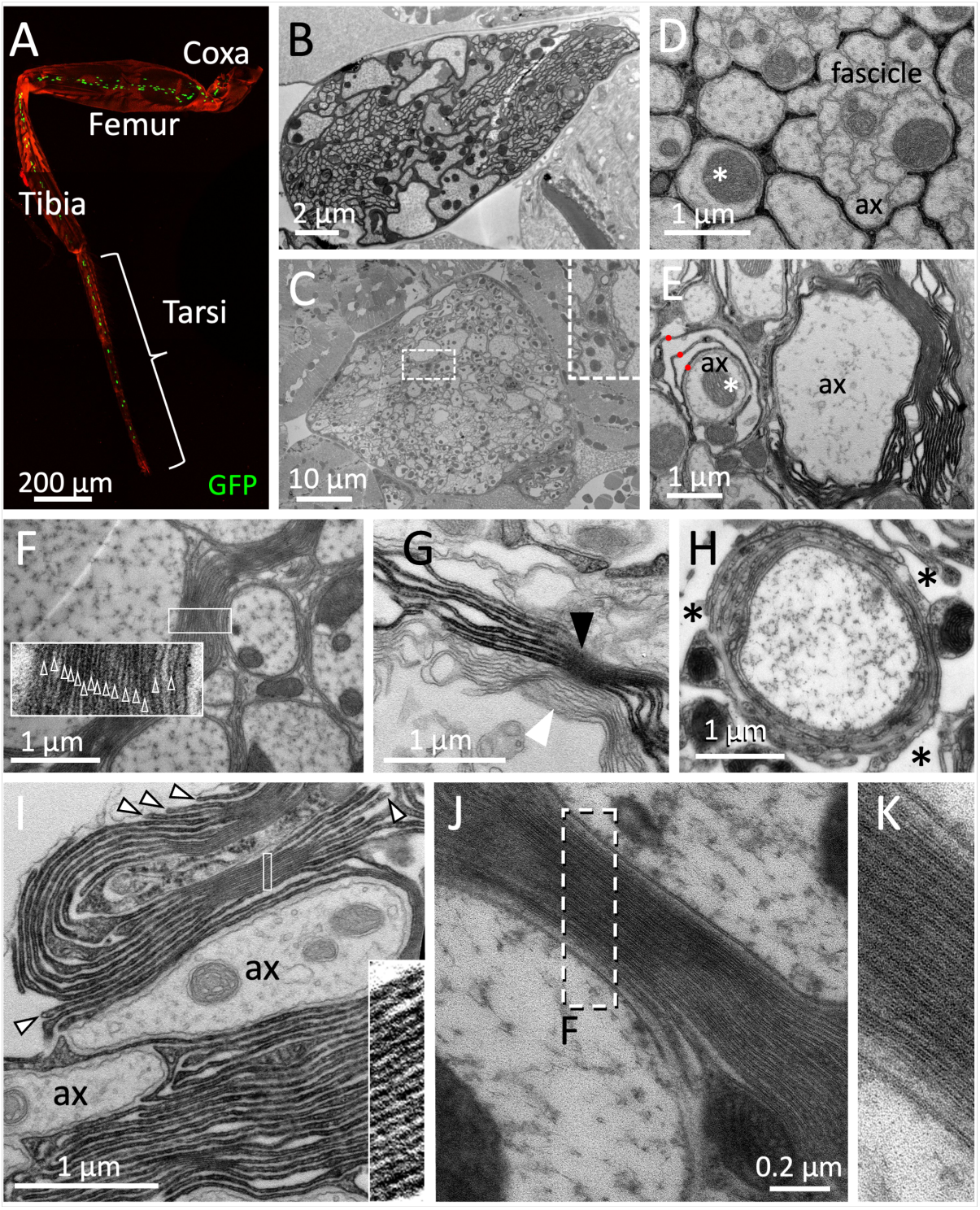
A
Coxa
Femur
Tibia
Tarsi
200 µm
GFP
B
2 µm
C
10 µm
D
fascicle
ax
1 µm
E
ax
ax
1 µm
F
1 µm
G
1 µm
H
1 µm
I
ax
ax
1 µm
J
F
0.2 µm
K

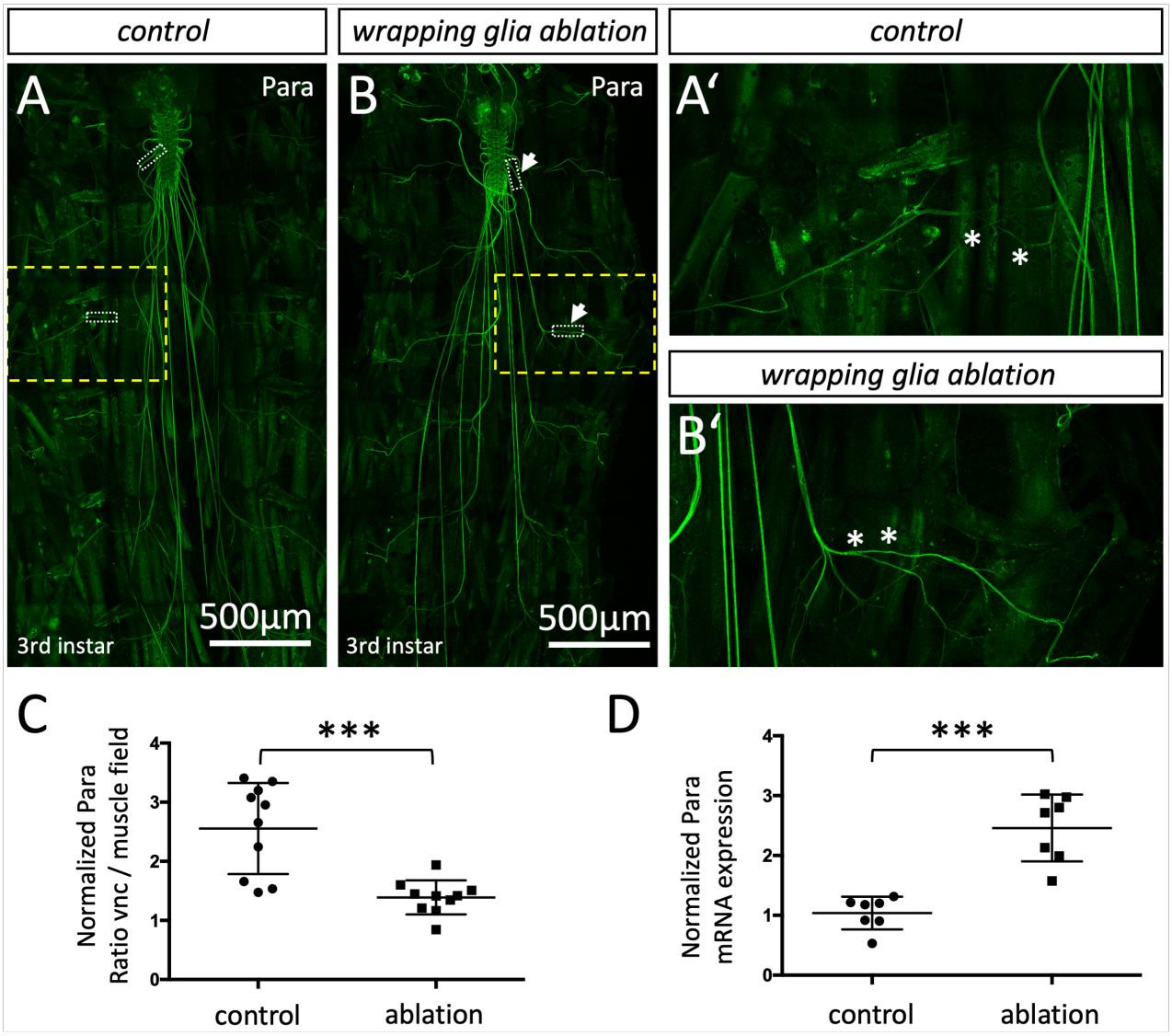
control
wrapping glia ablation
control
A
Para
3rd instar
500µm
B
Para
3rd instar
500µm
A'
wrapping glia ablation
B'
C
Normalized Para
Ratio vnc / muscle field
***
control
ablation
D
Normalized Para
mRNA expression
***
control
ablation

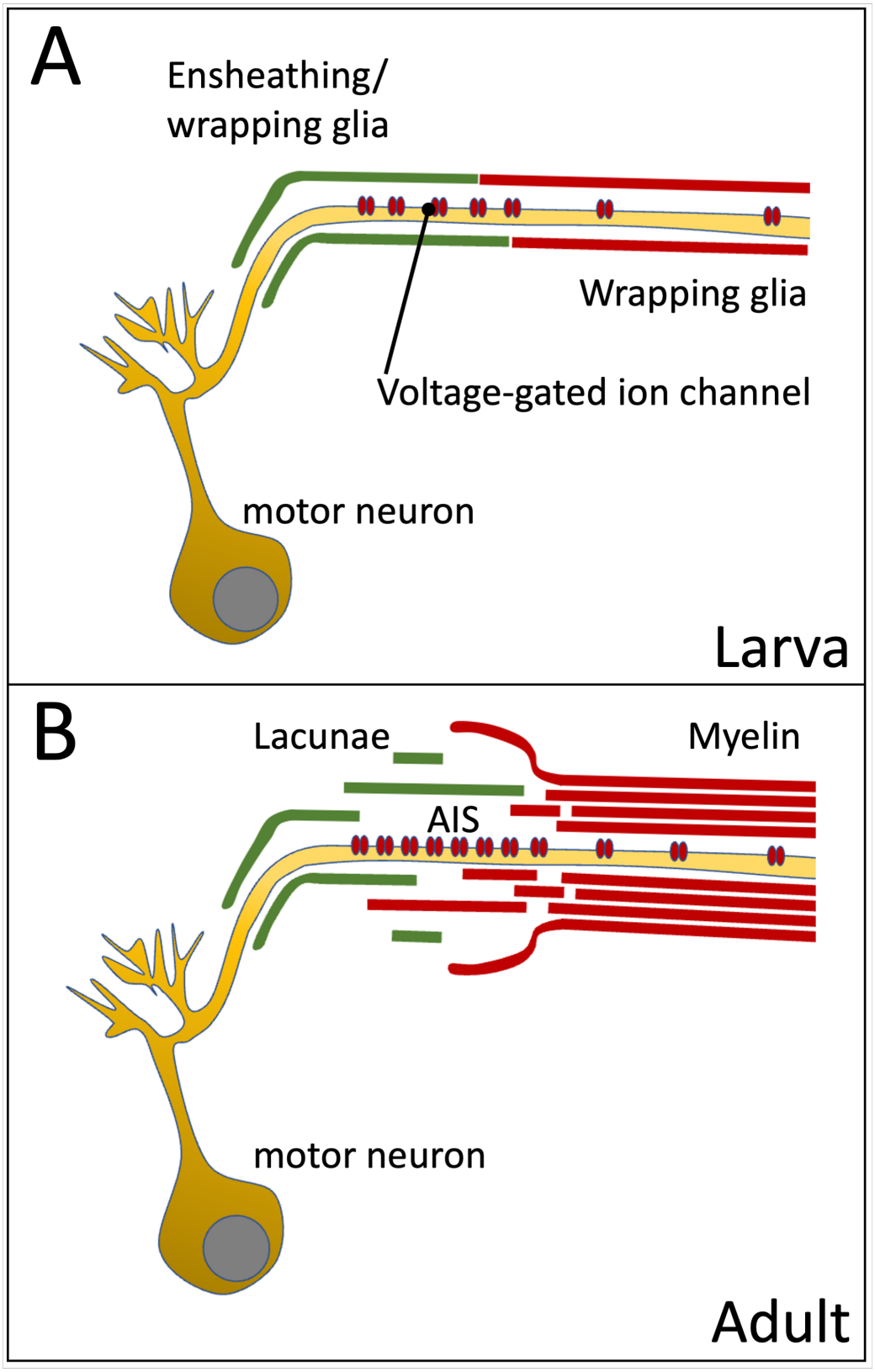
A
Ensheathing/
wrapping glia
Wrapping glia
Voltage-gated ion channel
motor neuron
Larva
B
Lacunae
Myelin
AIS
motor neuron
Adult